INVESTIGATING FUEL CLADDING COATING MATERIALS FOR ACCIDENT TOLERANT FUELS

A Dissertation

by

MILTIADIS DEMETRIOS KENNAS

Submitted to the Office of Graduate and Professional Studies of
Texas A&M University
in partial fulfillment of the requirements for the degree of

DOCTOR OF PHILOSOPHY

Chair of Committee,	K. Lee Peddicord
Co-Chair of Committee,	Lin Shao
Committee Members,	Pavel V. Tsvetkov
	K. Ted Hartwig
Department Head,	Michael Nastasi

May 2020

Major Subject: Nuclear Engineering

ABSTRACT

This study is a systematic investigation on the interface reactions of various coating materials for nuclear fuel cladding. In particular this study focused on metallic interdiffusion between these coatings and Zircaloy-4. The coatings used were $Fe_{70}Cr_{20}Fe_{10}$, Ti_2AlC, and pure Cr, applied via cold spraying. This study utilized various testing methods, including accelerator irradiation, SEM imaging, TEM imaging, micropillar compression, nanoindentation, and cantilever bending. The research performed is necessary for confirming phase diagram predictions, creating kinetic data to predict intermetallic growth rates outside of experimental conditions, and determining the impact, if any, to the long-term structural integrity of coated cladding.

It was found in the case of $Fe_{70}Cr_{20}Fe_{10}$ (FeCrAl) coating that the intermetallics Zr_3Fe and $(Fe,Cr)_2Zr$/ Fe_2Zr formed. Mechanical properties of these intermetallics indicated that they are harder and less ductile than the FeCrAl coating. Under ion irradiation, all intermetallics showed good void and swelling resistance, but the intermetallic $(Fe,Cr)_2Zr$ amorphized, potentially significantly impacting structural integrity of the coating-cladding interface.

In the Ti_2AlC-Zircaloy-4 system, the intermetallics Zr_3Al, ZrAl, and $ZrAl_2$ formed. In addition, precipitates of $(Fe,Cr)_2Zr$ were found in the Zr_3Al intermetallic. All intermetallics were tested to be less hard than Ti_2AlC. Under ion irradiation, Ti_2AlC, Zr_3Al, and Zircaloy-4 hardened. In addition, partial amorphization was noted in every intermetallic, and the $(Fe,Cr)_2Zr$ precipitates fully amorphized, consistent with the material's behavior in the FeCrAl-Zircaloy-4 system.

Investigating the materials property changes of the pure Cr-coated Zircaloy-4 proved to be challenging, as there was no discernible intermetallic formation and only a ~1.1 µm thick on average Cr diffusion zone into Zircaloy-4 was observed. The thickness of this diffusion zone saturated rapidly, making kinetic analysis inconsequential. The thin width of this diffusion zone combined with the lack of intermetallic formation made conventional micromechanical testing methods impossible or provide poor reproducibility. Ultimately this thin diffusion zone is unlikely to severely impact the structural stability of the Cr-Zircaloy-4 system.

DEDICATION

To my family, friends, mentors, and coworkers. Without any of them, this achievement would not be possible.

CONTRIBUTORS AND FUNDING SOURCES

This study was supervised by an advisory committee comprised of Dr. K. Lee Peddicord (committee chair), Dr. Lin Shao (committee co-chair and research PI), and Dr. Pavel V. Tsvetkov of the Nuclear Engineering Department, and Dr. K. Ted Hartwig of the Materials Science and Engineering Department.

Dr. Lin Shao provided guidance for experiment direction and greatly assisted with the manuscript preparation for the publications resulting from this research.

The Zircaloy-4 used in this research was provided by the Massachusetts Institute of Technology. The cold-spray method used to apply FeCrAl, TiAlC, and pure Cr to the Zircaloy-4 was performed by the University of Wisconsin-Madison.

TEM lamella preparation via FIB was performed by Hyosim Kim and Tianyao Wang. Jonathan Gigax and Hyosim Kim assisted and provided guidance during TEM imaging of the samples. Xuemei Wang and Jonathan Gigax assisted with operation and shift work of the 1.7 MV Ionex Tandetron ion accelerator used for sample irradiation. Jonathan Gigax performed micropillar fabrication for the samples used in Section 2, and performed the compression of these pillars. Aaron French performed micropillar fabrication of the samples used in Section 4. Hyosim Kim and Aaron French performed the EBSD mapping used in Section 4. All other work completed for the dissertation was completed by the student.

The study is supported by the US Department of Energy Integrated Research Project Grant # DENE0008416 and by the US Department of Energy through NEUP-IRP.

TABLE OF CONTENTS

LIST OF FIGURES

LIST OF TABLES

1. INTRODUCTION

1.1 Background

As research and development into the field of next-generation reactors progresses, there is strong emphasis on enhancing the accident tolerance of core fuel and structural components. In the wake of the 2011 disaster at the Fukushima-Daiichi Nuclear Power Plant, clear conclusions could be drawn from the performance of the Zircaloy-2 fuel cladding. Exposure to high temperature water following the loss of recirculating coolant to the spent fuel pools of reactors 1, 2, and 3 resulted in substantial buildups of hydrogen gas and subsequent chemical explosions (Figure 1 [1]). An implication to the performance of Zircaloy-4 in a loss of coolant accident (LOCA) is drawn as well: for

Figure 1. Chemical explosion at Fukushima-Daiichi following hydrogen buildup during a LOCA. Still frame captured from [1].

next-generation fuel to achieve superior accident tolerance, zirconium-based claddings cannot be directly exposed to water and steam that exceed standard reactor operation parameters. Logical progressions of this conclusion are clear: claddings must either not be zirconium-based, or claddings must be coated with material showing superior oxidation and corrosion resistance in LOCA conditions, with the focus of this dissertation being on the latter.

Developed as fuel cladding due to its low thermal neutron absorption coefficient, corrosion resistance, ductility, and hardness, Zircaloy is a suitable alternative to steels in light water reactors (LWRs). Zircaloy-4 was developed with lower nickel content than Zircaloy-2, with the intent being to reduce hydrogen uptake and slow the effects of hydride embrittlement and hydrogen-assisted stress corrosion cracking (HSCC).

Because of Zircaloy-4's nature to strongly oxidize in a water environment, its aggressive oxide scale formation leads to hydrogen formation at the coolant-cladding interface. Hydrogen has poor mobility in Zircaloy, and once the solubility limit of hydrogen in the Zircaloy is reached, zirconium hydrides begin to form. These hydrides are brittle and over long periods of time can fracture due to thermal stresses, leading to large crack propagation through the cladding [2, 3]. Hydrides form along the basal plane of the HCP structure of Zircaloy-4, and so the growth direction of hydrides can be predicted through the manufacturing process of Zircaloy-4 cladding. With the basal plane oriented circumferentially, hydrides form circumferentially, and when the basal plane is oriented radially, hydrides form radially [4]. Because the HCP structure is non-isotropic, the crystal tends to show a preferred orientation during cold working of the cladding tube. The preferred orientation can be determined using the Q value in Eq. (1). In Eq. (1), Q is a unitless value, t_0 and t are cladding wall thickness before and after cold work, respectively, and D and D_0 are cladding diameters before and after cold work, respectively.

$$Q = \frac{(t_0 - t)/t}{(D_0 - D)/D_0} \tag{1}$$

If the Q value is very small, the basal planes of the HCP crystals are oriented along the cladding's radial direction, and if the Q value is very large, the basal planes are oriented circumferentially. In order to minimize the possibility of hydride-induced cracking propagating through the cladding entirely, it is generally recommended that the basal planes should be oriented circumferentially, so the Q value is to be kept large.

Prospective coatings must largely maintain the desirable chemical and mechanical properties of Zircaloy-4, whilst also carrying suitable heat transfer between the fuel rods and primary coolant. Coatings must also extend the service and storage life of fuel cladding by reducing, eliminating, or at minimum not exacerbating the effects of creep, swelling, corrosion with coolant, hydrogen embrittlement, and HSCC. It is the combination of these factors in the relatively inexpensive cladding that currently limits the lifetime of the significantly more expensive nuclear fuel.

1.2 The Purpose of This Research

Three coating materials were supplied by the Massachusetts Institute of Technology (MIT) for investigation of mechanical and irradiation responses following high temperature annealing with Zircaloy-4: $Fe_{70}Cr_{20}Al_{10}$, hereafter referred to as 'FeCrAl' or 'Fecral,' the MAX phase Ti_2AlC, hereafter referred to as 'TiAlC' or 'MAX phase,' and pure chromium. Individually conducted studies into these materials seem to indicate promising results [5, 6], but testing in isolation may not provide the full picture for the feasibility of using these materials in a practical setting.

Thermal interdiffusion between the coatings and Zircaloy-4 can result in the growth of intermetallic compounds not initially present in the coating or substrate. These compounds will have differing ductility, melting points, grain and crystal structure, thermal conductivity, and radiation resistance to both coating and substrate. By forming layered rings between the coating and substrate, these intermetallics present a significant challenge to coating Zircaloy: a single intermetallic reacting poorly to the extreme temperature gradient induced by a LOCA or the continual neutron flux of standard lifetime operation can effectively create a 'weak link' in the ability of the coating to resist adhesive failure to the substrate.

The ability of selected coatings to strongly adhere to the zircaloy-4 substrate without adversely impacting the coating-cladding diffusion system is also of focus in this dissertation. The mechanism for adhesion cannot introduce a contaminant layer, and must be able to survive the extreme conditions of a high-flux, extended lifespan. A novel cold-spraying approach formulated by the University of Wisconsin-Madison (UWM) is the selected adhesive application of this dissertation [7]. The ideal implementation of this approach introduces no external contaminants to the system by relying solely on plastic deformation of the coating as the adhesive measure. Cantilever bending testing shown in Section 2, Subsection 2.3 indicates that cohesion between the substrate and coating supersedes the strength of the coating material, albeit with no consideration given to thermal interdiffusion or irradiation-induced effects to nanolaminar structures.

It must be noted that this dissertation does not aim to approve or deny the progression of research and development of any particular coating or adhesion process. It will not attempt to draw conclusions of the viability of coating Zircaloy-4 versus substitution of another cladding. It instead aims to provide focused insights into a limited scope of interactions between one cladding material and three selected coatings, adhered using one cold-spray formula, with the intent of directing future research into the conclusions drawn herein.

1.3 Use of Heavy Ions to Simulate Neutron Irradiation Response

Research into the radiation response of prospective coatings and of Zircaloy-4 has been routinely conducted, however there has been relatively little focus placed on coating-cladding interactions at expected reactor operating conditions. In particular, the effects of sustained radiation damage to intermetallic compounds created by thermal interdiffusion can be unclear in a large number of promising prospective coatings. This study aims at investigating the effects of radiation damage on these intermetallics, providing some insight into the suitability and practicality of selected materials in this application.

To this effect, heavy ion implantation is used as a surrogate to simulate neutron damage on intermetallics over the entire extended lifespan of such coated claddings. Specifically, 3.5 MeV Zr ion implantation to peak damage concentrations of 50-150 dpa is the basis of this investigation into the radiation resistance of the selected coatings. Though current LWR reactor cladding is limited to less than 10 dpa, next-generation designs will feature significantly higher neutron flux and extended lifetime fuel, making the 100 peak dpa figure realistic for consideration.

Heavy ions have a short penetration range with a large variation in dpa rate over the penetration depth. However, damage cascades induced by heavy ions are similar to those of neutrons [8, 9], therefore the near-surface region is the only region available for analysis. Additionally, heavy ion implantation generates significantly lower heat than neutron irradiation, allowing for higher dose rates and shorter irradiation times. Neutron-atypical effects do exist in ion implantation, however. The primary example of such an effect is a defect imbalance partially caused by interstitial-vacancy recombination in the peak ion deposition range due to implanted ions acting as injected interstitials and creating forward recoil of target atoms [10]. The end result of this defect imbalance is the suppression of void formation towards the end of the ion penetration depth; crucially this is a phenomenon that is not present in neutron-irradiated materialsZr was specifically selected for irradiation of the coated samples in order to minimize the chemistry changes of the material that is being implanted; in the case of this study, primarily Zr-based intermetallics were predicted to form.

1.4 The 1.7 MV Ionex Tandetron

The 1.7 MV Tandem accelerator used for the irradiations in this study was built by the General Ionex Corporation in 1983 and is currently operated by the Texas A&M Radiation Material Science Laboratory and Characterization Facility. The accelerator produced the ions used in this experiment via a Source of Negative Ions by Cesium Sputtering (SNICS) source.

The SNICS source uses a solid cathode machined out of the element intended for ionization, giving the flexibility of being able to ionize any element found in a solid form. This cathode is inserted into a high vacuum source head. Attached underneath the head is a small reservoir of liquid cesium, also kept at high vacuum to prevent the cesium from oxidizing or reacting to water vapor in air. When heated, the cesium vaporizes and travels upward into the source head, where it is deposited onto the cathode and onto an ionizing filament. The filament, when heated by passing electrical current through it, releases thermal electrons that are then accelerated in a spiraling path by a static electric field. On their spiraling path, these electrons have a high chance of interaction with cesium vapors. Owing to its weak electronegativity, cesium is very likely to positively ionize when interacting with these accelerated electrons. Positive cesium ions are then accelerated towards the cathode by an externally applied electric field. These accelerated cesium ions impact the surface of the cathode, sputtering away atoms of the desired material. The sputtered atoms travel through the cesium vapors and become negatively charged due to cesium's proclivity to give up electrons. The cesium previously deposited on the cathode by the heated reservoir enhances the likelihood of producing a negatively charged sputtered ion. These now negatively charged ions sputtered from the cathode are accelerated in the opposite direction of the positively charged cesium, towards a low energy steering magnet.

The steering magnet is necessary to act as a mass spectrometer. Any impurities on the surface or in the machining of the cathode will also be sputtered and ionized by the SNICS source, particularly oxygen from zirconium oxides on the surface of the zirconium cathode. Incoming ions of different mass and charge will bend with different radii through the same magnetic field, while ions of the same mass and charge will bend together. The steering magnet thus filters the outgoing beam from the SNICS source and allows the user to select the desired ion and charge state. In this study, specifically Zr^- ions were selected.

Following the steering magnet, the Zr^- ions pass into the accelerating electric field generated by a Cockcroft-Walton ladder driven by a pentode-based push-pull AC circuit. The 1.7MV is a 'tandem' accelerator, implying that the electric field is split between two acceleration columns. Both columns are positively charged with respect to the center, or 'terminal,' of the accelerator. Incoming Zr^- ions are first accelerated by the positive electric field towards the terminal. However, if left to continue, they would enter the opposite acceleration column and be accelerated backwards towards the same terminal. Therefore a charge exchange at the terminal must take place. A nitrogen electron-stripper gas is pumped into the terminal area of the accelerator, where the accelerated negative ions are 'stripped' of electrons by the nitrogen. The number of electrons stripped can be anywhere from 0 to the total number of electrons in all electron shells, however the yield of these stripped charge states decreases with increasing charge. For the purpose of this experiment, Zr^- ions that were stripped of three electrons to become Zr^{2+} are desired. The now positively charged ion beam passes from the terminal into the second acceleration column, where they are re-accelerated. The beam then enters the high-energy steering magnet.

Because the beam is now composed of multiple positive charge states of Zr ions, a single charge state must be selected to ensure only ions of the desired energy are allowed to reach the sample. These Zr ions enter a high-energy steering magnet following their reacceleration, and as was the case with the low-energy steering magnet, ions of the same charge state bend with the same radii, while ions of a different charge state bend with different radii. After pre-acceleration induced by the SNICS source, the first acceleration column, and the second acceleration column, the Zr^{2+} ions selected with the high-energy steering magnet possess 3.5 MeV of energy.

When considering that 1 MV of electric field accelerates a single-charged ion to 1 MeV, the capability of a 1.7 MV accelerator to produce 3.5 MeV ions is significant. It allows for higher energies to be reached than on single-ended accelerators, which are limited only to accelerating ions once, as opposed to twice. However, there is a drawback in that the nitrogen stripper gas charge exchange reduces the final beam current of the machine by a factor of approximately 10.

A significant component of the 1.7 MV accelerator system used by the Texas A&M Radiation Material Science Laboratory and Characterization Facility is the beam filtering system following the high-energy magnet. The entire beamline is kept at high vacuum (~5.0 E-7 torr), but impurities will still be present. As the beam passes through these impurities, it imparts columbic drag onto them, dragging these impurities towards the target and implanting them along with the desired ions. The effect is significant: the introduction of carbon through columbic drag can result in the formation of carbides in the near surface region. These carbides act as defect sinks, which have the effect of reducing ion-induced void swelling rates dramatically below the expected neutron-induced values [11].

To combat this, small steering magnets were placed along the beamline between the high-energy steering magnet and target chamber. As the beam passes through these magnets, it is mildly deflected back and forth within the beampipe until it reaches the target. Any impurities picked up by the beam will likely be lighter than the accelerated ions, and will be at a significantly lower energy. As a result these dragged-along impurities have significantly lower momentums than the accelerated ions, and will be deflected more than the ions. These impurities are deflected into the beampipe over the course of the beam filtering system, leaving the final beam impinging on the target nearly free of impurity, with the exception of those picked up past the final small steering magnet). To combat these final impurities, two liquid nitrogen cold traps were installed: one in the beamline with the filtering system, and one in the target chamber. When liquid nitrogen is poured into the traps, copper fins of high surface area within the beamline and chamber become cold enough to condense impurities onto their surface, preventing the impurities from being released back into the vacuum until the fins are allowed to return to room temperature. The combination of these measures was found to return ion-induced void swelling rates to that of neutron-induced void swelling rates [11].

2. FeCrAl-COATED ZIRCALOY-4[*]

FeCrAl has been considered as both a coating and as a complete replacement for Zircaloy-4 cladding. It shows superior corrosion resistance to Zircaloy-4 owing to its high Cr and Al content, promoting the growth of chromium and aluminum oxides. It has suitable strength, ductility, heat transfer, and melting point to be considered as a potential coating or cladding.

However, neutronics analysis points out that FeCrAl has a relatively high thermal neutron absorption cross section, especially when compared to that of Zircaloy-4 (2.43 barns for FeCrAl vs 0.20 barns for Zircaloy-4 [12]). As a result, replacing Zircaloy-4 with FeCrAl will require the new cladding to be approximately 10 times thinner to avoid a significant impact to core neutron economy. Despite FeCrAl's desirable mechanical properties, this solution is not feasible for PWRs or BWRs, though it may have merit in fast neutron flux reactors or in core systems using U_3Si_2 fuel instead of UO_2, owing to the higher uranium density [13].

Hydrogen has high solubility in Zircaloy-4, and when this solubility limit is reached, Zirconium hydride can begin forming through microcracks, embrittling the cladding and creating failure concerns for fuel pin at high stress during spent fuel cooling

---

[*] A part of this chapter is adapted with permission from C. Servant, C. Gueneau and I. Ansara, "Experimental and Thermodynamic Assessment of the Fe-Zr System," J. Alloys & Compds., vol. 220, p. 19, 1995, Copyright 2020 by Elsevier.

A part of this chapter is reprinted with permission from J. G. Gigax, M. Kennas, H. Kim, B. R. Maier, H. Yeom, G. O. Johnson, K. Sridharan and L. Shao, "Interface Reactions and Mechanical Properties of FeCrAl-Coated Zircaloy-4," J. Nucl. Mat., vol. 519, pp. 57-63, 2019, Copyright 2020 by Elsevier.

[14]. Another attractive benefit of FeCrAl as a coating is that hydrogen does not form stable hydrides with it, which allows the fuel to survive for longer periods in storage without the concerns of hydrogen-assisted stress corrosion cracking and long-term embrittlement. This is due to the higher mobility of hydrogen atoms in FeCrAl compared to Zircaloy-4 [2].

2.1 Experimental Procedure

No widely accepted process for the coating of fuel cladding has yet been implemented on a commercial scale. Due to the nature of thermal interdiffusion, and for the purposes of this research, a coating procedure in which contamination from an added layer of adhesives cannot be selected. Additionally, the coating itself must be uniform in thickness, largely free of porosity, and avoid alternation of the chemical or mechanical properties of the material being coated. An attractive method for coating the substrate is the cold-spraying approach applied by UWM [7, 15]. This approach was selected as it satisfies the requirement of no introduced adhesive, and as it is a cold approach, it maintains the original chemical and mechanical properties of the coated material.

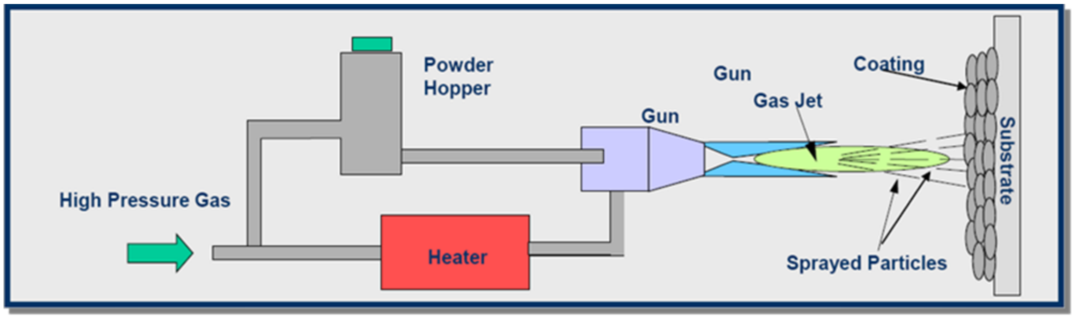

Figure 2. Layout of the cold-spray system used by the University of Wisconsin-Madison. Reprinted from [15].

It is noted that for FeCrAl coated Zircaloy-4, this method apparently introduces a carbon contamination of currently unknown origin between the coating and substrate. This contamination existed prior to irradiation. This approach also introduces a small amount of porosity in the coating layer. However, a negligible level of porosity or cracking near the interphase region was observed after annealing in the regions of interest. It is currently unclear if any of these observed defects along the coating and interphase region were due to annealing or pre-existing defects from the fabrication process.

Zircaloy-4 samples were prepared by surface roughening with 320 grit SiC paper to remove surface oxidation and promote adhesion by increasing surface area, then were

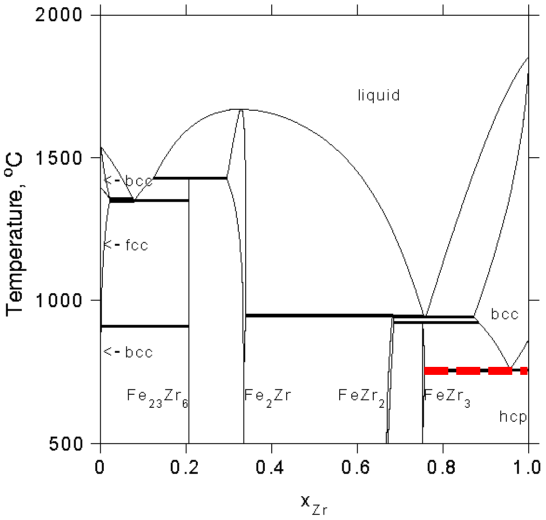

Figure 3. Phase Diagram of the Zr-Fe system. Dashed red line shows phase transition to be avoided. Adapted with permission from [16] Copyright 2020 by Elsevier.

sonicated in pure ethanol to dislodge surface particulates. FeCrAl particles smaller than 25 μm were cold-spray coated to the Zircaloy-4 surface using a CGT Kinetik 4000/34 commercial cold spray system. High-pressure nitrogen carrier gas at 750 °C was used to accelerate the powder through a tungsten carbide De Laval nozzle [7].

Upon receiving the coated stock, the samples were sealed within a high vacuum (~1.0E-6 torr) environment created by sealing a quartz tube plugged into a high vacuum chamber via oxy-propane torch. The tube was then placed in a furnace; samples intended for ion implantation were annealed at 998 K for 336 hours. Samples intended for diffusion kinetics analysis were annealed at 923 K and 963 K for 336 hours, and 998 K for 168 h and 336 h, respectively. All samples were heated and cooled at a rate of 10 °C/min. These temperatures were specifically selected in order to promote the most rapid interdiffusion possible while avoiding the α-Zr to β-Zr phase change at 1030 K, noted by

Figure 4. Mechanical polishing apparatus used for sample preparation.

the dashed red line in Figure 3 [16]. Following annealing, the samples were extracted from the quartz and mechanically polished along the cross-sectional face with 1200-grit SiC paper with ethanol lubrication, then polished again with a finishing pass of 0.25 µm glycol-based diamond solution. Ethanol lubrication was used to minimize surface oxidation of the zircaloy-4. The final glycol-based solution was selected because there is no approach for analyzing this particular coating, for example Electron Backscatter Diffraction (EBSD), that requires ultra-fine (~0.05 µm) polishing, and this solution is not water-based, in order to resist oxidizing the polished zircaloy-4 surface for as long as possible. Figure 4 shows the polishing apparatus used for this mechanical polishing.

A TESCAN LYRA-3 gallium focused ion beam (FIB) was used to fabricate micropillars in the coating, intermetallic phases, and Zircaloy-4 substrate, cantilevers extending across the as-received coating-substrate interface, and 100nm-thick transmission electron microscopy (TEM) lift-outs.

Micromechanical testing to study the mechanical properties of the intermetallic phases was performed using a Hysitron TI950 Triboindenter, equipped with a flat-punch probe for micropillar compression and a Berkovich tip for nanoindentation across the interdiffusion region. Cantilevers were loaded via Berkovich tip at a constant load rate of 20 µN/s up to a peak force of 10 mN. Micropillars were compressed via constant strain rate of $4.0\text{x}10^{-4}$ s^{-1} to a peak strain of 30%. The interdiffusion region was nanoindented via low-load transducer equipped with Berkovich tip, loaded to a peak force of 5 mN.

Scanning electron microscopy (SEM) imaging was performed using a FEI Quanta 600 scanning electron microscope equipped with a backscatter electron detector (BSED) and energy dispersive X-ray spectroscopy (EDS) detector. TEM imaging was performed using a FEI Tecnai T20 transmission electron microscope equipped with an EDS detector. Point defects are difficult to see in TEM lamella specimens, so the main focus of the TEM microscopy is to provide better resolution on intermetallic formation than is possible through SEM, to look for the formation of voids in the near-surface region of the material due to irradiation-induced vacancy clustering, and comparing the diffraction patterns of crystalline structures before and after irradiation.

Ion irradiation was performed using a 1.7 MV Ionex Tandetron ion accelerator. Ion bombardment was targeted towards the cross-sectional face, and used Zr^{2+} ions accelerated to 3.5 MeV. The Zr ion was selected in order to minimize chemistry changes in the substrate and intermetallic regions. Zr ions were selected in favor to Fe ions as iron diffusion into zirconium was predicted through diffusion kinetics calculations, while Zr diffusion is largely negligible. As a result, intermetallics were predicted to be Zr-based. The projected ranges of 3.5 MeV Zr into Zircaloy-4 and FeCrAl were shown by the simulation software Stopping Range of Ions in Matter (SRIM) [17] to be ~1.0 µm and ~800nm, respectively. Because of these limited penetration ranges, the cross-sectional face was targeted for implantation, as opposed to the surface of the coating. Simulations used the Kinchin-Pease Model, suggested for accurate modeling of damage recently by Shao et. al. [18]. Samples were mounted via water-based silver paste to the surface of an Inconel hot stage and heated to 425 °C. Samples were irradiated to peak damage levels of 50, 100, and 150 dpa.

2.2 Intermetallic Formation

In order to understand the mechanical property shifts and irradiation response of the FeCrAl coating, proper identification of the intermetallic phases created with the zircaloy-4 substrate is critical. Our approach towards identification consists of consulting

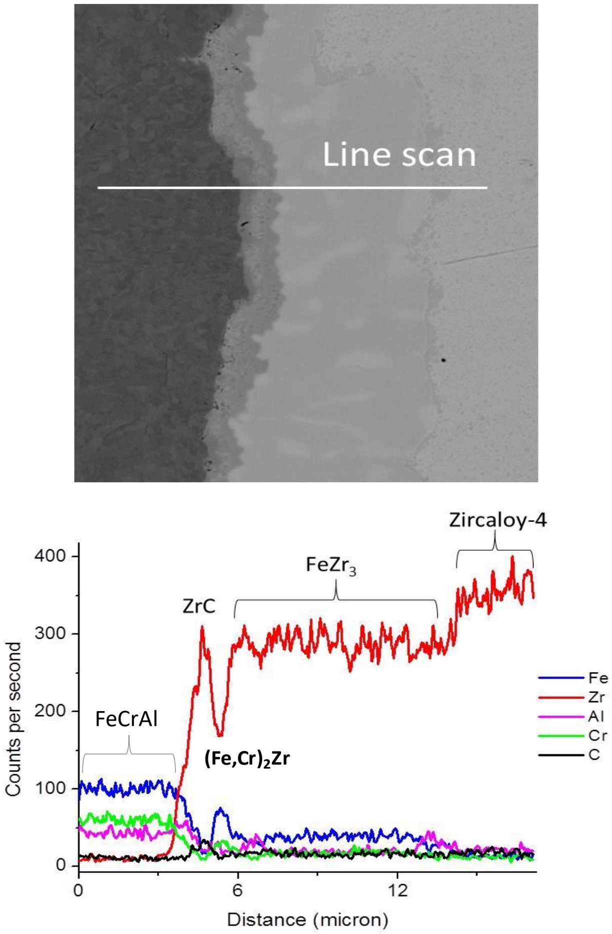

Figure 5. BSED image of the interface between FeCrAl (left) and Zircaloy-4 following annealing for three weeks at 725 °C, and an SEM-EDS line scan of this interphase.

known phase diagrams of the iron-zirconium diffusion couple system, SEM-EDS point and line scans, and verifying the SEM-EDS scans with further STEM-EDS point and line scans.

Despite FeCrAl containing three elements, EDS scans of the annealed sample show that Fe is the dominant diffusing element. Both Cr and Al diffuse into the interface reaction zones but no show no indication of reaching the Zircaloy-4. Al does not impact phase formation but can occasionally be found enriched at certain grain boundaries. Zr from Zircaloy had negligible diffusion inside the FeCrAl coating. Intermetallic phase formation is thus most governed by Fe diffusion into Zircaloy.

Figure 5 shows an SEM-EDS line scan across the post-annealing interface of FeCrAl (pictured left) and Zircaloy-4. Of note is the discontinuity of Zr and Fe atomic

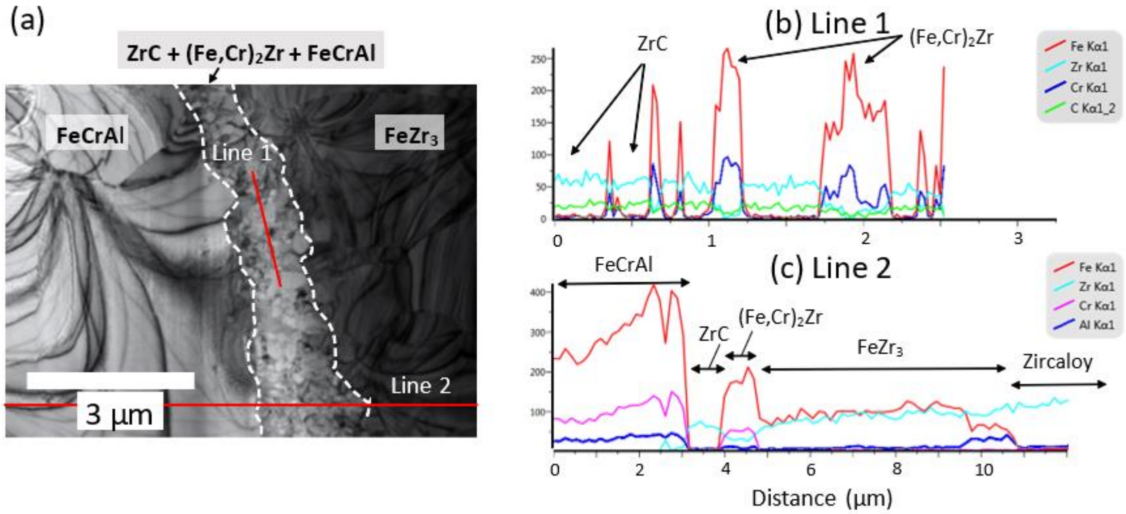

Figure 6. (a) STEM image of the mixed grains phase of the FeCrAl/ Zircaloy-4 interface region. (b) STEM-EDS line scan 1 along the mixed grains phase. (c) Line scan 2 across the mixed grains phase.

compositions across the interface region at the phases labelled ZrC and $(Fe,Cr)_2Zr$. This discontinuity is explained through the introduction of very small grains (~20-50nm diameter) of ZrC as a result of the carbon contamination introduced through the cold-spray process. These grains appear to break up continuous grains of $(Fe,Cr)_2Zr$ and FeCrAl in the interface region. Figure 6a shows a STEM micrograph of this broken up region, Figure 6b shows a STEM-EDS line scan along this region, and Figure 6c shows a STEM-EDS scan across it. Both Figure 6b and Figure 6c reinforce the discontinuity shown in the SEM-EDS data of Figure 5. The data presented in Figure 5 and Figure 6 are visually summarized in Figure 7. The complex overlap of mixed, small grains of ZrC, FeCrAl, and $(Fe,Cr)_2Zr$ results in EDS point scans of this region roughly identifying the stoichiometry of Fe_2Zr as an approximate composition of the entire mixed-grains phase. The compositions of the identified phases are tabulated in Table 1. Note that in Table 1, Fe_2Zr (mixed) specifically refers to this mixed-grains phase.

Table 1. Intermetallic phase compositions and thicknesses of FeCrAl-coated Zircaloy-4. Sample annealed at 998 K for 336 hours. Fe_2Zr and ZrC share the same phase.

Compound	**Zr (at %)**	**Fe (at %)**	**Cr (at %)**	**Al (at %)**	**C (at %)**	**Sn (at %)**	**Thickness (µm)**
FeCrAl	0	69.4	20.5	10.1	0.0	0.0	--
ZrC	57.5	0.6	0.0	0.0	41.9	0.0	2.259
Fe_2Zr	29.5	52.9	15.6	2.1	0.0	0.0	2.259
Zr_3Fe	72.2	27.6	0.1	0.1	0.0	0.0	8.945
Zircaloy-4	98.0	0.7	0.0	0.0	0.0	1.3	--

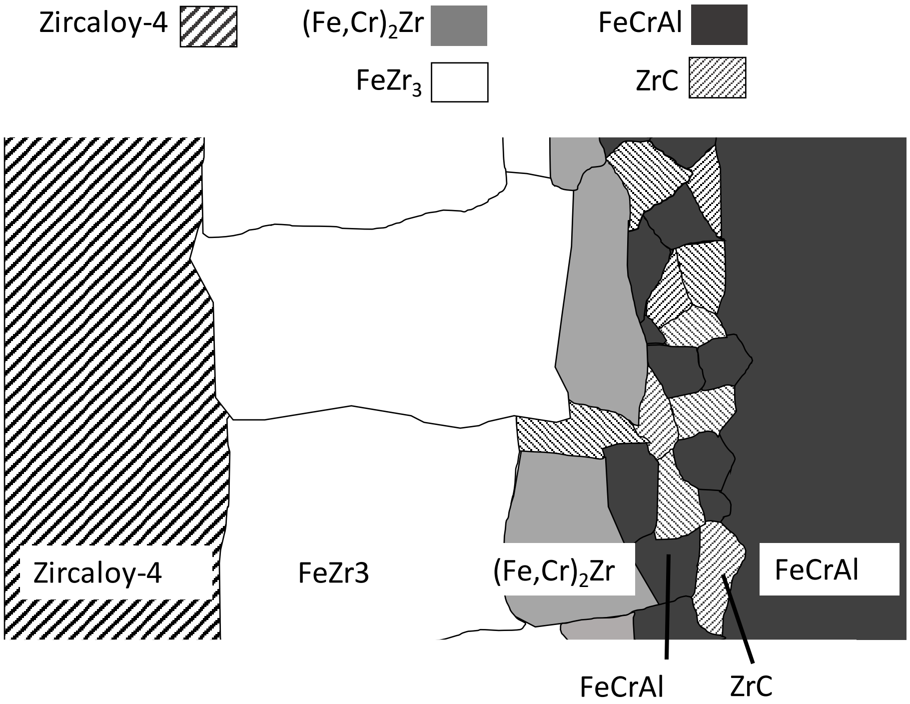

Figure 7. Graphical depiction of the Zircaloy-4, FeCrAl interface region.

Further confirmation of the existence of these phases can be found in the diffraction patterns obtained through TEM imaging of the area (Figure 8). Diffraction patterns extracted from the Zircaloy-4 substrate, FeCrAl coating, and $FeZr_3$ intermetallic phase show the clear crystallographic structures expected of these materials (HCP, BCC [19], and Re_3B-type orthorhombic [20], respectively). However, the mixed phase grains show overlapping polycrystalline diffraction patterns, making indexing or definitive identification of the individual patterns impossible. Despite this, the overlapping diffraction patterns provide further evidence of the existence of multiple compounds within the same phase. Additionally, the lack of diffuse returns from the diffraction patterns indicate that the cold-spray process did not result in solid-state amorphization.

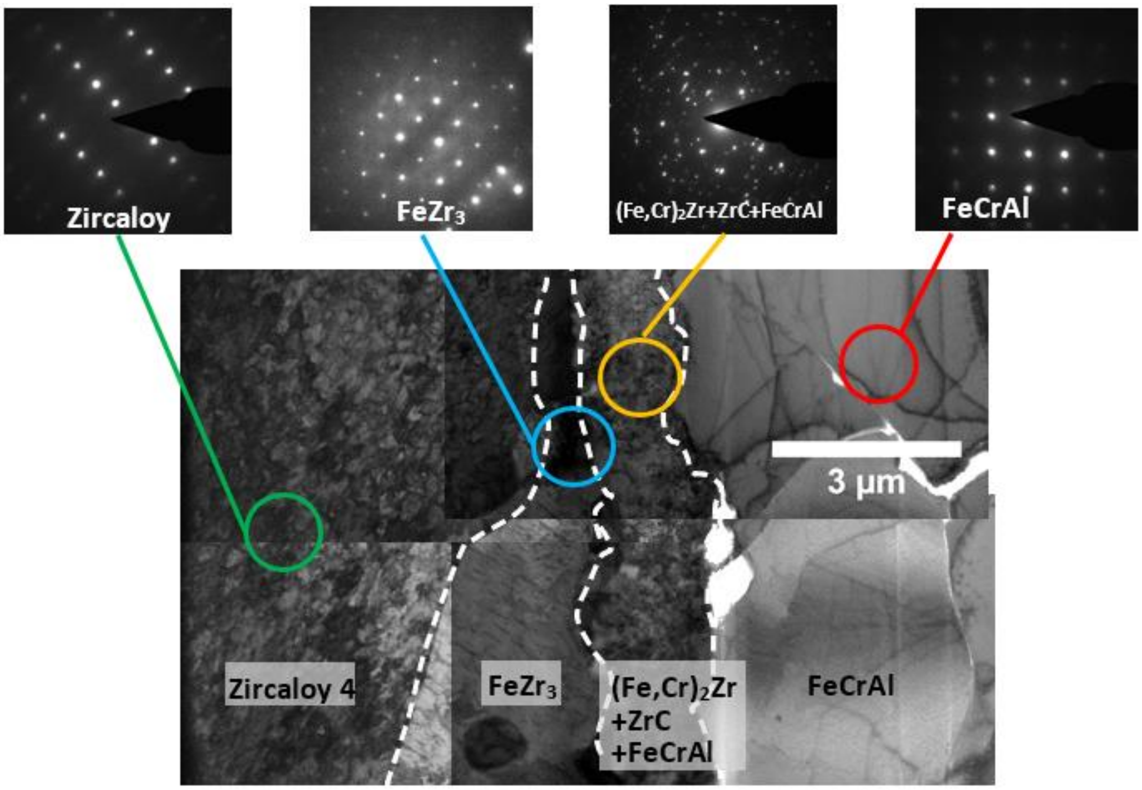

Figure 8. TEM micrograph of the interphase region. Diffraction patterns of Zircaloy-4, $FeZr_3$, mixed grain, and FeCrAl coating shown overhead.

Previous work [21] shows interdiffusion and interphase region formation could be facilitated by initial interface mixing due to cold spray bombardment. SEM-EDS scans showed that an ultra-thin interface zone formed in as-received samples. This has the effect of reducing the incubation period for interdiffusion. The effect of this incubation period will be further explored in the following section.

2.3 Diffusion Kinetics and Mechanical Properties

Phase widths in the FeCrAl-Zircaloy-4 system were measured via SEM imaging and compared against annealing temperature and duration to extract the integrated interdiffusion coefficient and intrinsic parabolic growth constant. Interfacial diffusion analysis will typically use the Boltzmann-Matano formulae assuming concentration gradients in the system are large enough [22]. However, in the case of this research the compositional differences between the intermetallic phases are too narrow for Boltzmann-Matano. Thus, the Wagner approach to calculate interdiffusion coefficients will be followed [23]. With the assumption that the concentration gradient in any given phase is constant, the integrated interdiffusion coefficient can be calculated by Eq.(4) [21, 23]:

$$\widetilde{D}_i^{Int,v} = \frac{(N_i^v - N_i^{-\infty})(N_i^{+\infty} - N_i^v)}{\left(N_i^{+\infty} - N_i^{-\infty}\right)} \times \left[\frac{(\Delta x^v)^2}{2t}\right] + \frac{\Delta x^v}{2t}\left[\frac{N_i^{+\infty} - N_i^v}{N_i^{+\infty} - N_i^{-\infty}} \times \int_{-\infty}^{x^{v-}} (N_i - N_i^{-\infty})\, dx + \frac{N_i^v - N_i^{-\infty}}{N_i^{+\infty} - N_i^{-\infty}} \times \int_{x^{v-}}^{+\infty} (N_i^{+\infty} - N_i)\, dx\right] \tag{2}$$

where N_i^v is the mole fraction of element *i* in phase *v*, $N_i^{-\infty}$ and $N_i^{+\infty}$ are the mole fractions of element *i* at the ends of the diffusion couple, Δx^v is the width of phase *v*, and t is the annealing duration.

If each intermetallic phase is considered the result of adjacent phases interacting at its boundaries, Eq. (2) can be simplified to Eq.(3), which shows the intrinsic parabolic growth constant to be written as [21]:

$$k_{ii}^v = \left[\frac{(\Delta x^v)^2}{2t}\right]_{N_i^{-\infty}=N_i^{v-1},\ N_i^{+\infty}=N_i^{v+1}} \tag{3}$$

where N_i^{v-1} and N_i^{v+1} are the mole fractions of element i in the adjacent phases. Eq. (2) can then be simplified to Eq. (4) [21]:

$$\widetilde{D}_i^{Int,v} = \frac{(N_i^v - N_i^{v-1})(N_i^{v+1} - N_i^v)}{(N_i^{v+1} - N_i^{v-1})} \times \left[\frac{(\Delta x^v)^2}{2t}\right] \tag{4}$$

Figure 9 shows the result when plotting Eqs. (3) and (4) by taking the average phase thicknesses and anneal times and plotting against the inverse of temperature. The activation energies for the Fe_2Zr and Zr_3Fe were measured to be 65.4 ± 9.01 and 58.1 ± 13.5 kJ/mol, respectively [21]. It should be noted that the activation energy of Zr_3Fe,

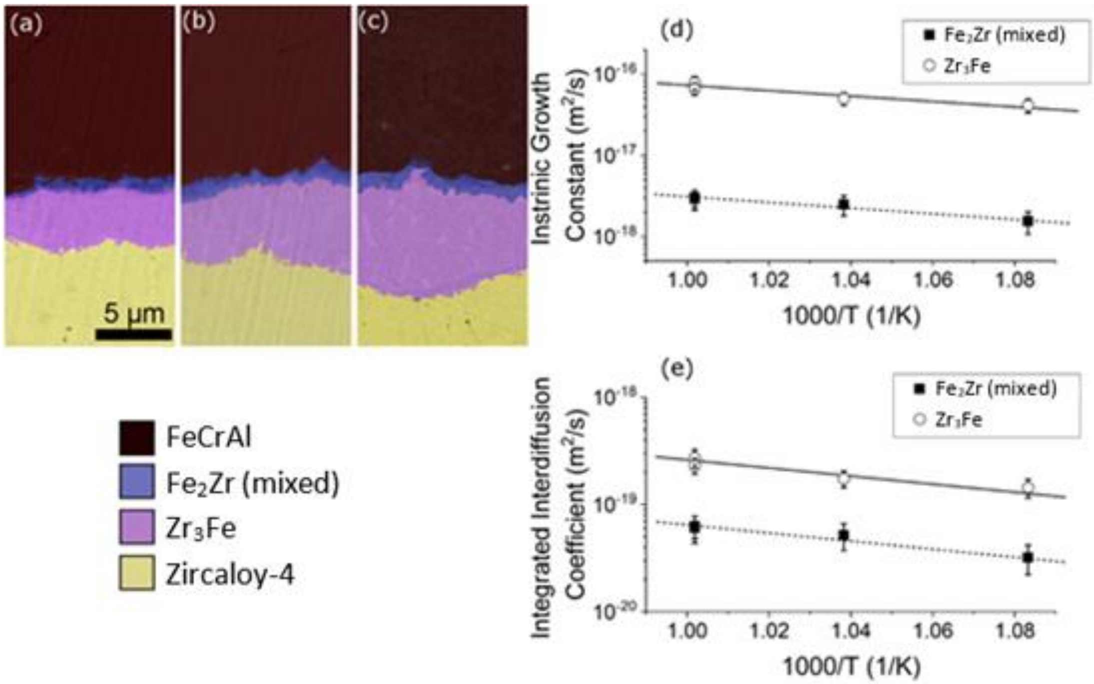

Figure 9. SEM micrograph of the FeCrAl-Zircaloy-4 system following annealing at (a) 923 K, (b) 963 K, and (c) 998 K for 336 hours. (d) Intrinsic growth constant and (e) integrated diffusion coefficients plotted against inverse temperature. Reprinted with permission from [21] Copyright 2020 by Elsevier.

when measured from a binary Fe-Zr diffusion couple, is 120 kJ/mol [24]. The discrepancy between this finding and that of previous literature may be the result of diffusion directly between coating and substrate introduced by the cold-spray process. This diffusion would lower the incubation period as previously mentioned in the previous section. Additionally, the removal of the oxide layer while surface roughening in preparation for the cold-spray may also correspond to the apparent drop in activation energy.

In order to remain a viable method for the deposition of a coating on to zircaloy-4, the adhesive strength accounting from the plastic deformation of deposited coating particles along the surface of the substrate must sufficiently withstand mechanical failure at the interface. This adhesive strength was tested via mechanical bending of cantilevers fabricated on the non-annealed, non-irradiated samples. Figure 10a shows a typical [25] fabricated cantilever. Figure 10b and Figure 10c show cantilevers following loading from a nanoindenter equipped with a flat punch probe. The light-colored portions of the cantilevers are Zircaloy-4 and the dark sections are the FeCrAl coating. As this method is intended to test adhesion strength and not coating structural strength, Zircaloy-4 was selected as the body of the pillar in order to prevent the possibility of structural failure of the cantilever due to the coating technique. Figure 10d indicates a large range of behavior from the loading of the cantilevers, however an overall conclusion can be drawn that the adhesion of the interface is stronger than the bonding within the coating itself [21]. Although cohesion between the substrate and coating supersedes the strength of the coating material, no consideration was given to thermal interdiffusion or irradiation-induced effects to nanolaminar structures.

Nanoindentation was performed in order to assess the micromechanical strength of the intermetallics compared against the coating and substrate. Because all samples were polished along their cross section, all phases were accessible to the probe without the need for multiple samples at differing polishing depths. Figure 11a shows the load displacement curves of the coating, substrate, and each intermetallic phase, and Figure

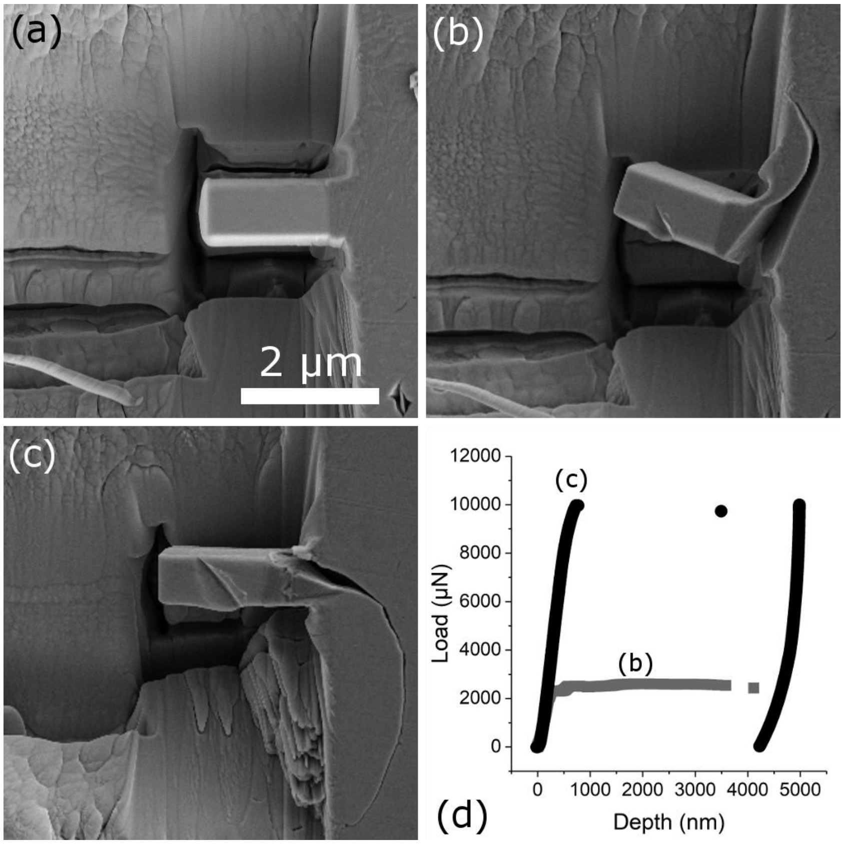

Figure 10. Mechanical bending of cantilevers. Light regions correspond to Zircaloy-4, dark regions correspond to FeCrAl. (a) shows SEM micrograph of typical cantilever. (b) and (c) Cantilevers following loading. (d) Load vs displacement plots of cantilevers (b) and (c). Reprinted with permission from [21] Copyrght 2020 by Elsevier.

11b shows hardness values extracted from these curves using the Oliver-Pharr method [26]. It is clear that both intermetallic phases are harder than both the coating and substrate. This is to be expected. In the case of Fe_2Zr, it is a mixed grain phase consisting in part of ZrC crystals, which as a result of their brittle ceramic nature increase the relative hardness of this phase compared to all others. Additionally, this phase has a narrow average width, and therefore some hardening could result from dislocation pileup at its interfaces. Lastly, because both the mixed grains phase and Zr_3Fe have differing grain structures to both each other and to the coating and interface, this is also a source of enhanced hardening due to lattice mismatch.

Of note as well is considering the higher degree of error in measuring the

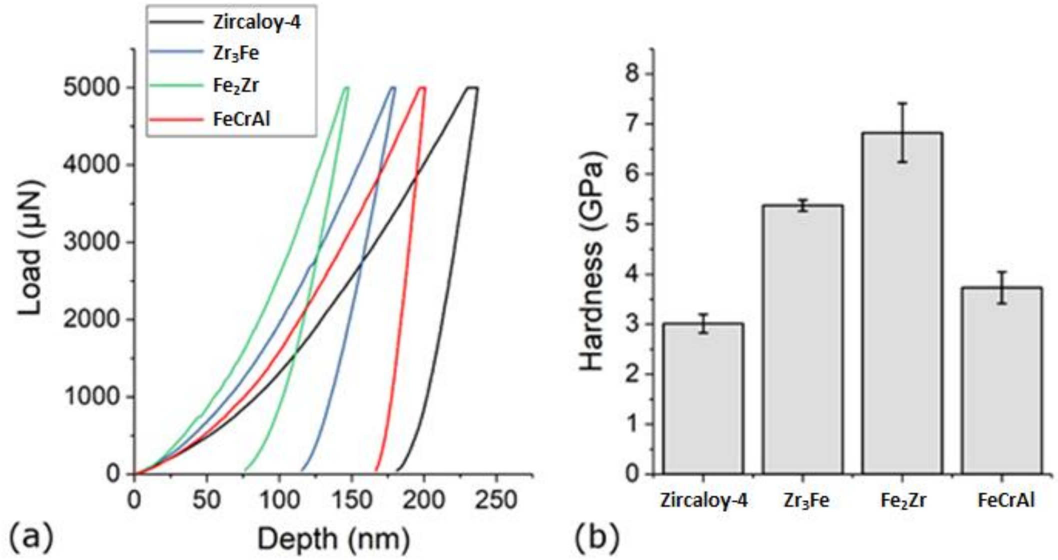

Figure 11. (a) Load-displacement curves for coating, substrate, and intermetallics. (b) Average hardness values of each phase. Reprinted with permission from [21] Copyright 2020 by Elsevier.

hardnesses of Fe_2Zr and FeCrAl compared to Zr_3Fe and Zircaloy-4, shown in Figure 11b. For Fe_2Zr, this is likely the result of the mixed grains present in the phase, as the probe itself (~10μm) is larger than the mixed individual grains (~20-50nm), making the indentation potentially inconsistent depending on the concentration of the various sub-phases at the indention site. In the case of FeCrAl, later TEM images show a degree of porosity in the coating as a result of the cold-spray process. This porosity is likely the result of inconsistencies in the readings.

Micropillar compression tests were performed to assess the compressive yield strength and plastic flow behavior of each phase. Pillar size was chosen based off the thickness of the Fe_2Zr mixed phase. From Table 1, this thickness is shown to be

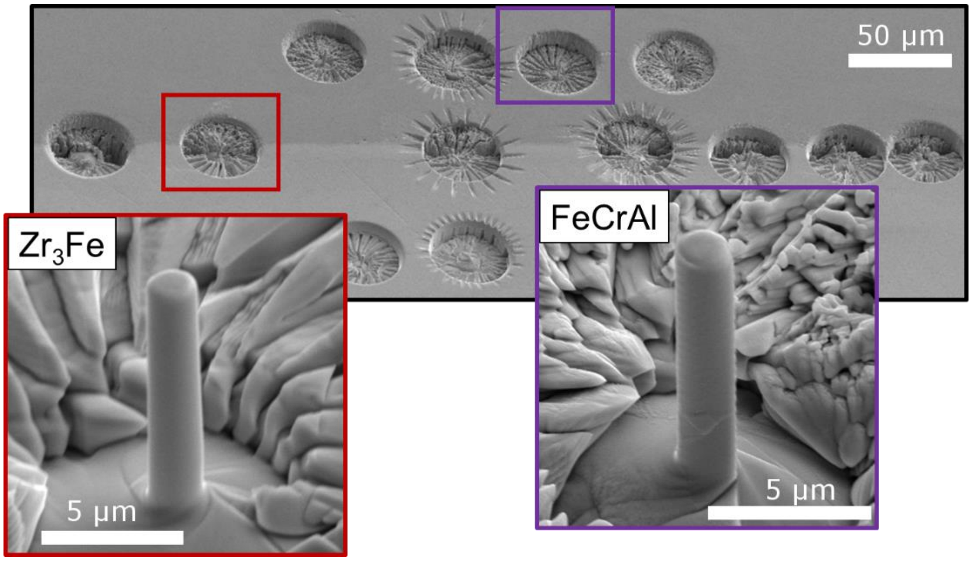

Figure 12. SEM Micrograph of Micropillars fabricated on the FeCrAl-Zircaloy-4 system. The location along the interphase region can be seen in the top image. Reprinted with permission from [21] Copyright 2020 by Elsevier.

approximately 2.0 µm, thus a pillar diameter of 1.75 µm was selected, with the exception of Zircaloy-4, in which both 1.75 µm and 3.0 µm pillars were used to generate data. In order to facilitate a fracture mode of failure (as opposed to lattice slip, which is utilized in the Cr-coated samples), the pillar height was made to be approximately 6.0 µm tall, resulting in an aspect ratio of 3.4:1.

Originally, pillars fabricated through conventional annular ion milling show a significant taper from peak widening to base. This complicates the fracture mode of failure, as different phases would be expected to fail at different heights along the pillars.

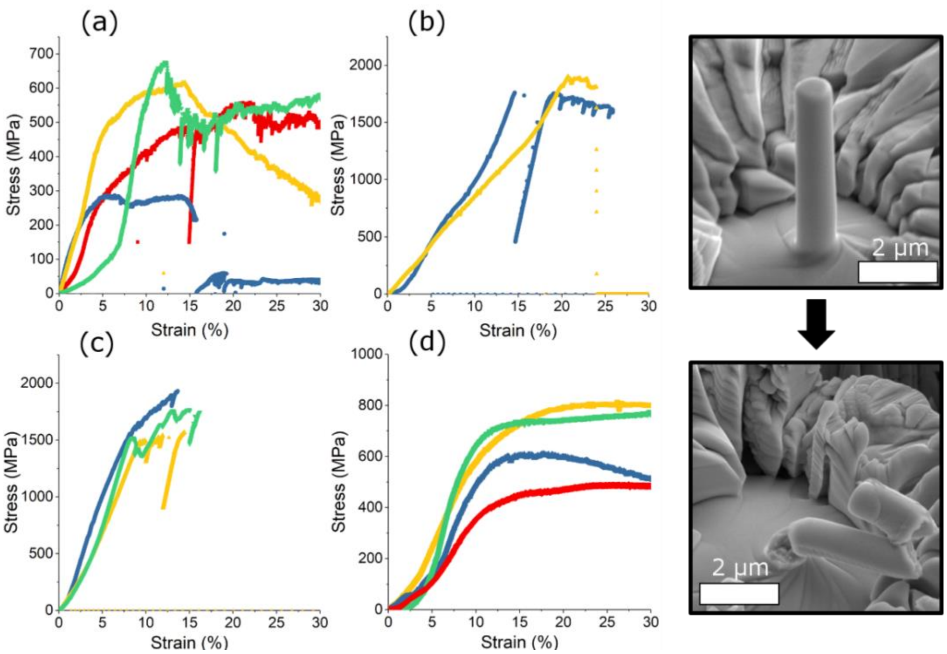

Figure 13. Micropillar compression stress-strain curves of the (a) FeCrAl, (b) Fe_2Zr, (c) Zr_3Fe, and (d) Zircaloy-4 regions. An SEM micrograph of a Zr_3Fe pillar before and after compression is shown next to the plots Reprinted with permission from [21] Copyright 2020 by Elsevier.

To address this, an ‘ion lathe’ [25] approach was taken, in which the focused ion beam sputters away flat portions of the annular face of the pillar. The pillar is then rotated, sputtered, and this process repeated until a smooth, round, taper-free final pillar is created. Figure 12 shows two examples of micropillars fabricated in FeCrAl and the Zr_3Fe phase. The pattern at the base of the pillars is indicative of the ion lathe approach.

Figure 13(a-d) show the micropillar compression stress-strain curves for the FeCrAl coating, Fe_2Zr (mixed) and Zr_3Fe intermetallic phases, and the Zircaloy-4 substrate, respectively. The stress-strain curves for FeCrAl (Figure 13a) show varying behaviors during compression. Results generally indicate brittle failure is favored. The yield strength was measured to be 400 ± 175 MPa [21]. The large range of yield strengths and fracture strains is an indication of the effects caused by enhanced density of grain boundaries and porosity introduced by the cold-spray process [21].

The compression stress-strain curves for the mixed phase are given in Figure 13b. Results on this phase remain unclear, as over repeated attempts on this region, only two of the pillars originally fabricated did not fail at low stresses (<300 MPa) and low strain (<5%) [21]. From this obtained data, it is clear that yield strength and elastic modulus are significantly higher when compared to FeCrAl, likely due to the presence of ZrC crystals. The absence of a plastic deformation zone indicates the phase showed a brittle failure mode at relatively low deformation before fracture.

Figure 13c shows compression stress-strain curves of Zr_3Fe. The yield strength of Zr_3Fe pillars (~1600 MPa) was similar to the successful Fe_2Zr pillars (~1800 MPa) [21]. The steeper elastic region of the curves indicates a stiffer elastic response compared to the mixed phase. Again, the preferred failure mode of the pillars was indicated to be brittle due to the lack of a significant plastic deformation zone. Despite this, some plastic deformation was observed shortly before fracture, but to a much lesser degree than the extent of the plastic deformation in Zircaloy-4.

As mentioned, pillars with diameters of 1.75 µm and 3.0 µm were fabricated in Zircaloy-4. The purpose of this was to compare how pillar diameter influenced mechanical response, with the intent that perhaps some conclusions could be drawn from wider pillars had the mixed phase been significantly thicker. From Figure 13d, the yellow, green, and blue curves are obtained from 1.75 µm pillars, while the red curve is generated from compression of the 3 µm diameter pillar [21]. Typical uniaxial tensile measurements of Zircaloy-4 indicate yield strength of 300-450 MPa [27]. From the data in Figure 13d, the 3.0µm pillar showed good agreement to the value reported by Argonne National Laboratory (ANL) [27, 28]. However, the thinner 1.75 µm pillars showed significantly lower yield strengths, indicating that this selected pillar diameter implies there is an impact from size effects. As was expected, Zircaloy-4 pillars showed substantially more deformation than other phases owing to its relative ductile nature. It was not observed to fracture for all pillars constructed.

The observed size effects of the Zircaloy-4 pillars may have troubling implications for the rest of the compression data obtained in the other phases. However, pillars in the coating material and intermetallic phases may not be impacted by the relatively limited volume of their pillars. This is because grain sizes of FeCrAl and the intermetallics are significantly smaller than that of Zircaloy-4.This creates one or more grain boundaries in the pillars that help promote fracture in a similar vein to small volume single-grain pillars, as the nearby surface to the small volume helps to replicate the dislocation nucleation and interaction that grain boundaries do [29, 30]. It is clear that the FeCrAl pillars contain at least one such grain boundary as evidenced by the lack of a ductile failure mode that would be expected of the material given its mechanical properties [31].

From the findings of the nanoindentation, cantilever bending, and micropillar compression, a qualitative understanding of the material responses of FeCrAl, Zircaloy-4, and their intermetallic phases to annealing can be garnered, and some implications towards the viability of the cold-spray process can be made. The final coating approach should, ideally, not significantly alter chemical or mechanical properties of the material being sprayed. The results displayed from Figure 13d imply that the failure mode of FeCrAl has shifted from ductile in isolated investigation [31] to brittle [21]. The results of Figure 10 indicate the cold-spray approach has good adhesive strength of coating to substrate in non-annealed samples. Further investigation into this adhesive strength in the cases following annealing and particularly following irradiation (as the next section will show amorphization under ion irradiation of the $(Fe,Cr)_2Zr$ component of the mixed grains phase) is recommended. The results of Figure 11 have shown that both intermetallic phases have shown higher hardness than the substrate and coating, and Figure 13 indicate a brittle failure mode of these intermetallic phases. Crucially, these phases fracture very shortly after reaching yield strength. These properties introduced by annealing are indicative of potential ‘weak links’ in the overall coating-cladding-fuel package that isolated investigation of FeCrAl [31] could not otherwise determine.

2.4 Irradiation Response of Intermetallics

The irradiation response of FeCrAl alloys have already been well documented [5], however there has been little focus on the irradiation response of any intermetallic phases created between itself and Zircaloy-4. Quantifying the radiation response of intermetallic phases is often complicated, and should be approached differently from bulk analysis. This is because interphase compounds are generally compressed between other phases, contain many defects, and are typically polycrystalline with very small grains (making the extraction of a TEM diffraction pattern complicated, as shown in Figure 8). The combination of these factors potentially introduces a vulnerability of structural collapse, in particular delamination of the coating from substrate, after irradiation.

Following irradiation on the cross-sectional face to 50, 100, and 150 peak dpa, the most immediately significant observation under TEM was the amorphization of part of the mixed grains phase. Figure 15a shows a TEM micrograph of the amorphized region, with Figure 15b showing a diffraction pattern obtained from within this supposedly amorphized region. The amorphous rings and total lack of visible diffraction patterns are indicative of full amorphization. Figure 15c is an STEM micrograph of the same location as in Figure 15a, and shows the performed location of the EDS line scan in Figure 15d. The inset damage plot indicates that the amorphous region exists only in the irradiated near-surface region. No amorphization was noted in samples that were annealed but unirradiated, therefore this amorphization is entirely irradiation-induced.

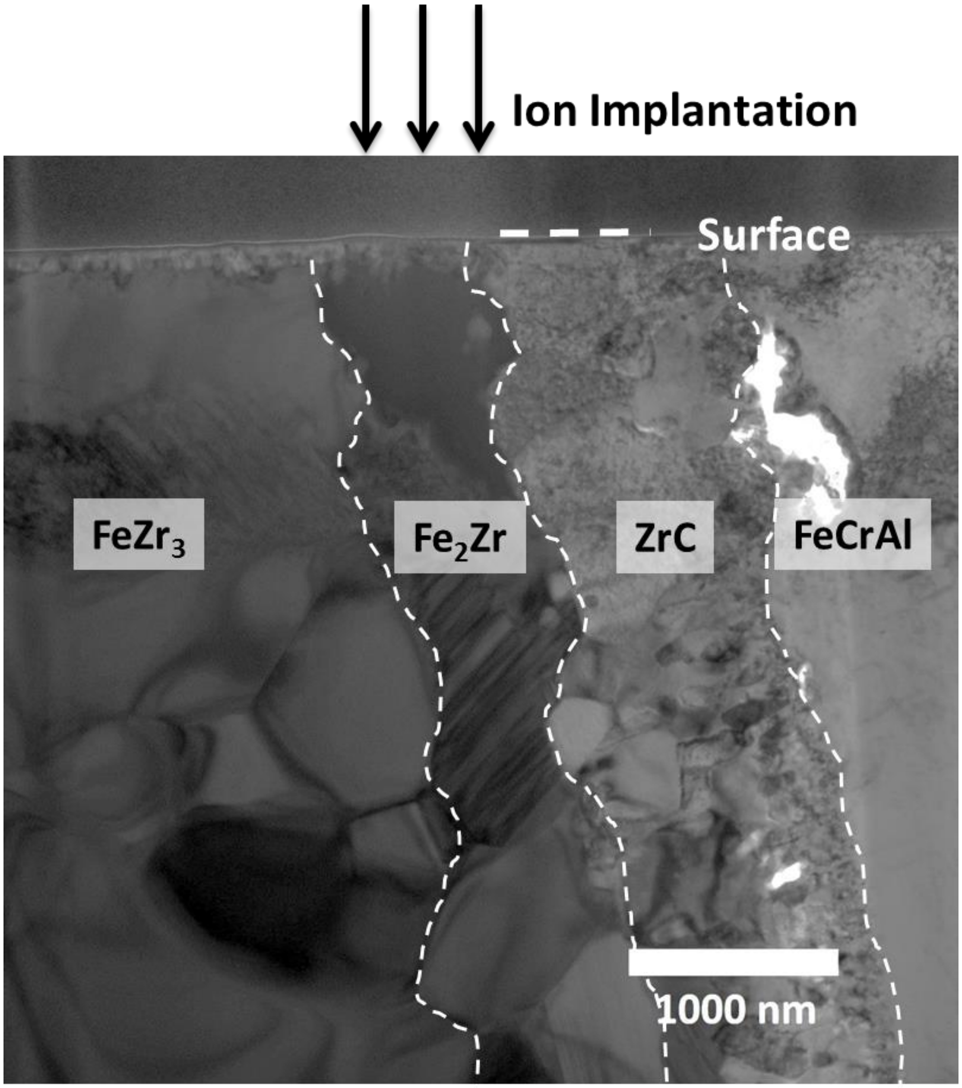

Figure 14. TEM overview of the 150 dpa FeCrAl-coated sample at the intermetallic diffusion zone near the FeCrAl interface.

Although up to this point $(Fe,Cr)_2Zr$ has been considered as part of the Fe_2Zr mixed grains phase, what has been noted through EDS point and line scans is that this compound consistently and preferentially exists between $FeZr_3$ and ZrC/FeCrAl. Were it not for some occasional interruptions due to grains of FeCrAl or ZrC, $(Fe,Cr)_2Zr$ could

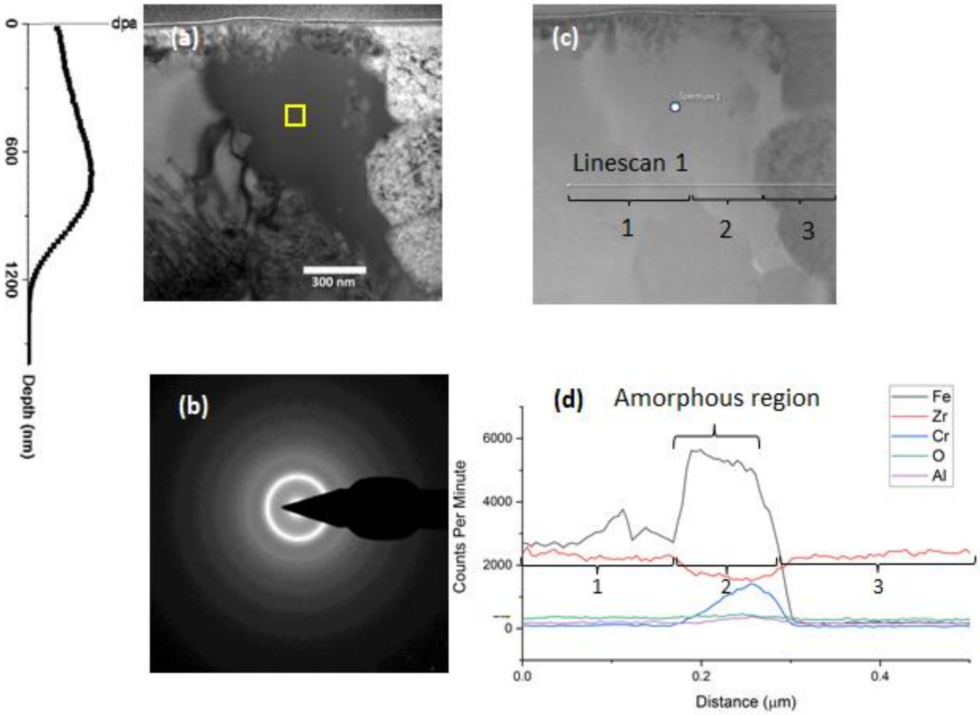

Figure 15. (a) TEM Micrograph of the amorphized region. (b) Diffraction pattern taken from the yellow square in (a). (c) STEM micrograph of the same region as in (a). (d) EDS Line Scan taken across the amorphous region in (a) and (c). Damage plot inset at left of (a).

essentially be considered its own continuous phase. Refer to Figure 7 for a graphical interpretation of the location of this intermetallic.

TEM micrographs of the 50, 100, and 150 dpa samples indicated the amorphous region of Figure 15a consistently exists between $FeZr_3$ and ZrC/FeCrAl. The line scan of Figure 15d shows three distinct regions: region 1 is the Fe, Zr-rich grain of $FeZr_3$, region 2 is the Fe, Cr, and Zr-rich (though Zr is relatively depleted compared to its immediate neighbors) amorphous region, and region 3 is a Zr-rich grain of ZrC. Figure 16 reinforces the EDS line scan data from Figure 15 and shows direct comparisons within and beyond the irradiation range. Data of the EDS point scans taken of the amorphized region and its surroundings (Figure 16) are tabulated in Table 2. Comparing the data from these scans to the data from Table 1, it is clear that the $(Fe,Cr)_2Zr$ phase is what amorphized under irradiation.

There are a significant number of studies that have shown the ability of $(Fe,Cr)_2Zr$ to amorphize under irradiation [32, 33, 34, 35], and is later shown again in Section 3, Subsection 3.4 presenting as precipitates in the Zr_3Al intermetallic of the TiAlC-coated

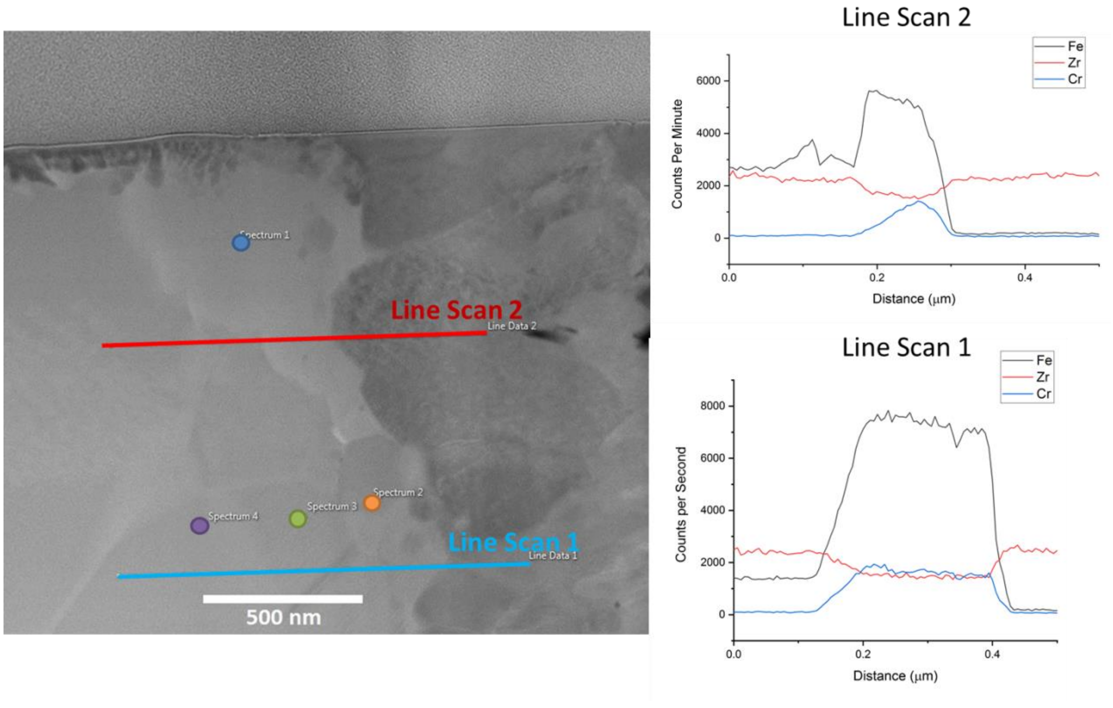

Figure 16. STEM-EDS scanning overview of the amorphous region of the 150 dpa sample, with corresponding EDS line scans shown to the right. EDS point scan data shown in Table 2.

.

Zircaloy-4 system. $(Fe,Cr)_2Zr$ has a high glass formation capability, and its ability to be fabricated through mechanical alloying or melt-spinning methods implies that the critical cooling rate for metallic glass formation is significantly lower than other metals or alloys. Defects introduced by irradiation damage can increase local system energy and help promote $(Fe,Cr)_2Zr$ into a metastable glassy state. However, ion irradiation has been able to cause recrystallization of amorphous materials due to elevation of the system energy beyond this metastable state, then allowing the system to minimize energy by relaxing into a crystal structure [36]. This is not always the case, as ion irradiation can also introduce local melting and superfast quenching, allowing the amorphized state to stabilize [37, 38].

Table 2. EDS point scans for regions indicated by the dots in Figure 16.

Point	**Blue**	**Purple**	**Green**	**Orange**
Fe at %	45.6	20.6	40.0	42.4
Zr at %	34.3	60.7	25.3	25.6
Cr at %	11.7	3.3	11.3	9.5
Al at %	2.9	8.3	1.8	2.1
C at %	5.5	7.1	21.6	20.4

Despite the introduction of ZrC as a result of potential contamination during the coating or cold-spray surface preparation, it is not expected to significantly affect overall structural integrity. At roughly 2.3 µm thick on average, the ZrC layer is likely thin enough so as to not act as a thermal insulator for heat transfer between the cladding and coating. It has been found to have electron conductivity similar to that of metals [39].

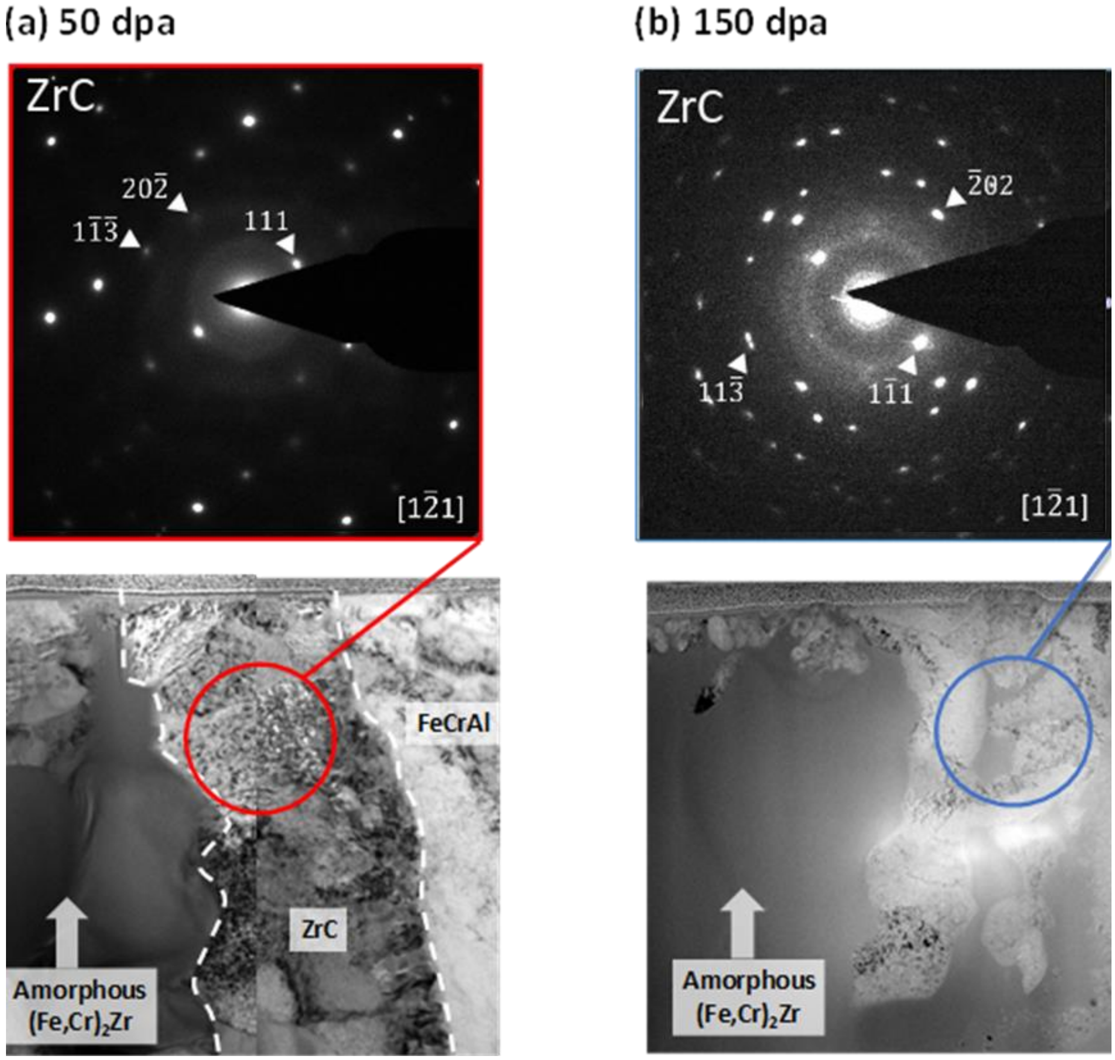

Figure 17. (a) Diffraction pattern of ZrC and the near-surface region it was taken from in the 50 dpa sample. (b) Diffraction pattern of ZrC and near-surface region it was taken from in the 150 dpa sample.

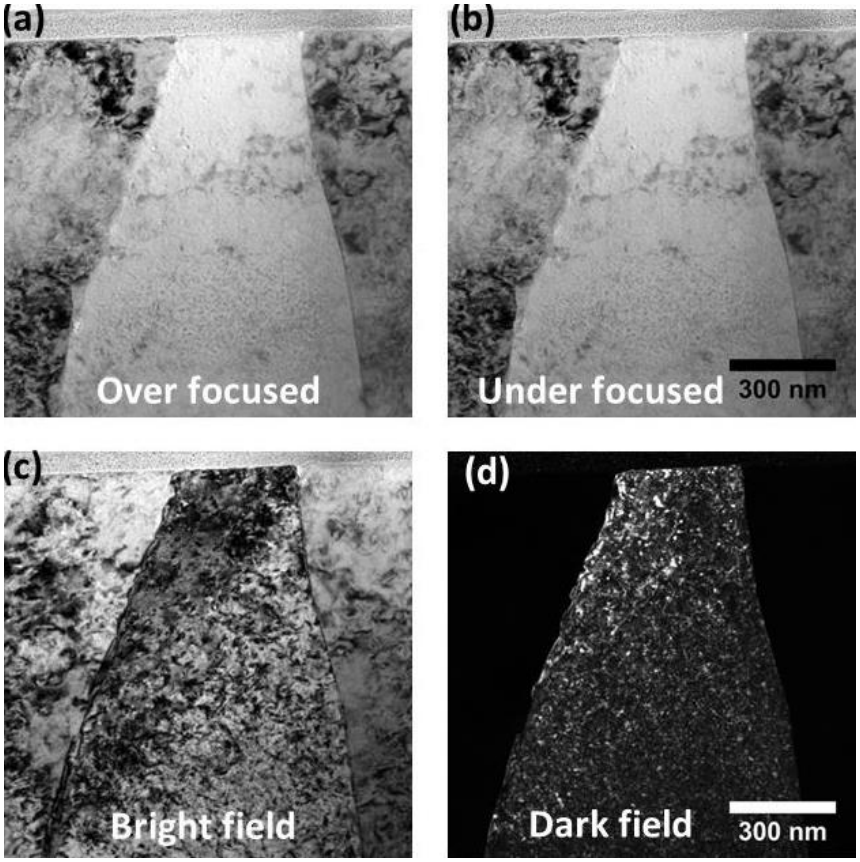

Figure 18. (a) Over-focused, (b) under-focused, (c) bright field, and (d) dark field TEM images of FeCrAl irradiated to 150 dpa.

The crystal structure of ZrC is B1(NaCl), and it has two face-centered sub-networks of C and Zr. The C sub-network has a high vacancy density because ZrC is sub-stoichiometric by nature. The radiation tolerance of sub-stoichiometric ZrC was found to exceed that of nearly stoichiometric ZrC [40]. This is because the high vacancy density results in good resistance to defect propagation as the vacancies provide recombination sites for displaced C atoms during irradiation [41]. The observations from the work in this dissertation are consistent with these prior studies.

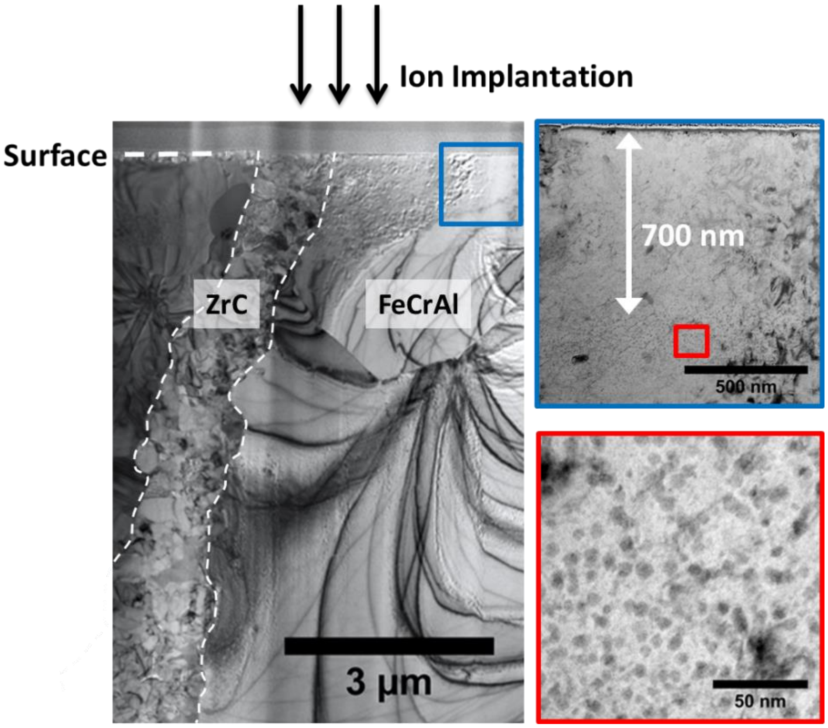

Figure 19. TEM image of the FeCrAl coating region. Blue box shows an enhanced view of the near-surface region. Red box shows an enhanced view of the precipitation in the near-surface region.

It was noted from the diffuse ring in the diffraction pattern in Figure 17b that ZrC apparently partially amorphized under high dose (150 peak dpa), but from the diffraction pattern in Figure 17a it showed no signs of partial amorphization at the lower dose (50 peak dpa). The partial amorphization is likely due to overlap between ZrC grains and the amorphous $(Fe,Cr)_2Zr$. However, in previous work with Au heavy ion irradiation on ZrC, amorphous diffraction rings were observed as well. But in this case, Zr-based nano-precipitates inside the ZrC were the likely cause of the diffuse ring [41]. Given these considerations, it can be concluded that the ZrC in the FeCrAl-coated Zircaloy-4 samples was not amorphized.

Figure 18a and Figure 18b show over-focused and under-focused TEM images of the FeCrAl coating, respectively, following 150 dpa irradiation. From the absence of black dots and white dots in the near-surface regions of Figure 18a and Figure 18b, respectively, it is evident that no voids have formed. Note that there are black dots present towards the bottom of both of these figures. These dots are attributed to ion-irradiation induced precipitation of Zr atoms, as these precipitates occur only within the peak ion deposition range and not in the peak damage (near-surface) region. High-density dislocations are observed in both the bright field (Figure 18c) and dark field (Figure 18d)

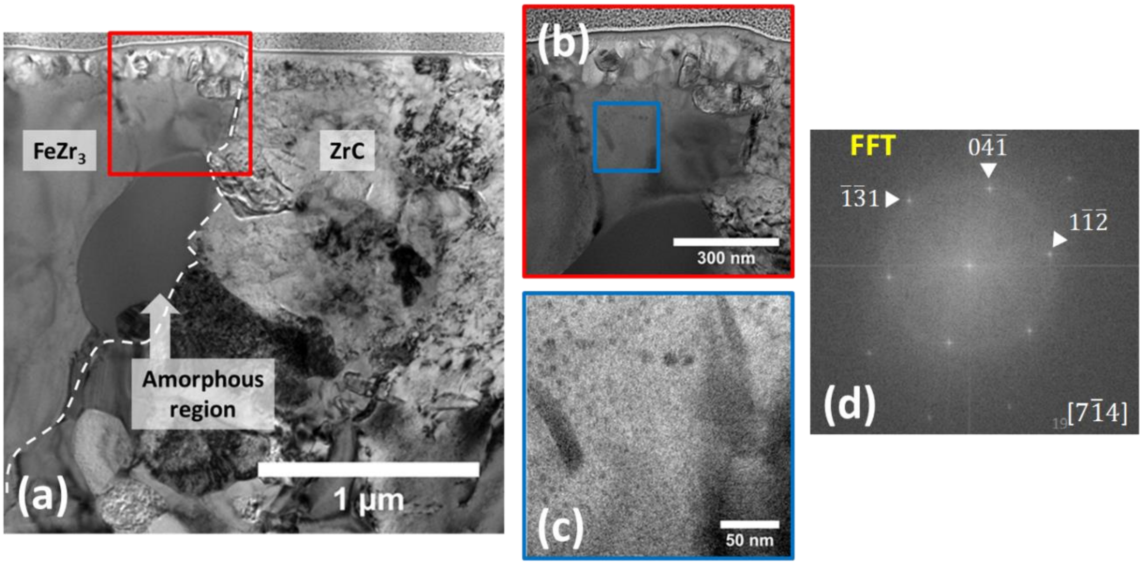

Figure 20. (a) TEM image of the FeZr$_3$ phase near the (Fe,Cr)$_2$Zr/ ZrC interface. (b) Enlarged image of FeZr$_3$ in the near surface region. (c) Further enlarged image of this region. (d) Indexed FFT of FeZr$_3$.

images of the FeCrAl coating. Early systematic studies on Kr ion-irradiated FeCrAl show formation of interstitial type $< 100 >$ dislocations and mixed interstitial and vacancy type $\frac{1}{2} < 111 >$ dislocations [42]. This observation is generally rare in ferritic systems, suggesting a high mobility of vacancies [42]. This likely explains the lack of void growth, as the high efficiency of vacancy removal aids in their annihilation and increases opportunities for interactions with defect sinks.

Figure 19 shows a TEM overview of the FeCrAl coating after 100 peak dpa. The blue box shows an enhanced view of the near-surface ion irradiated region. No white dots are indicative of the lack of void formation. The red box shows an enhanced view of

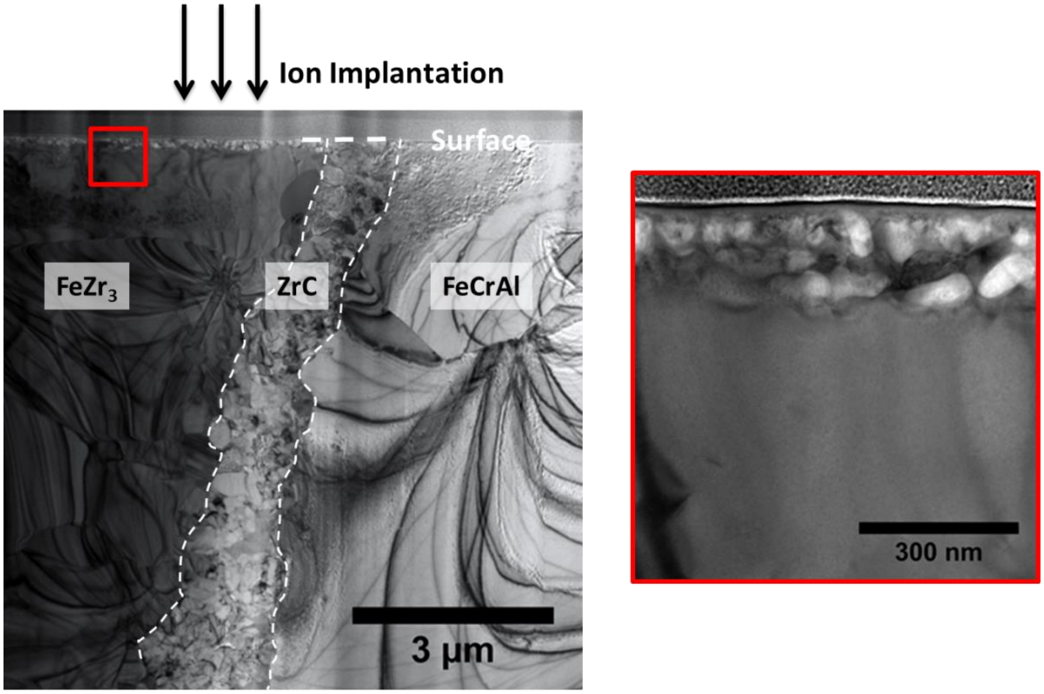

Figure 21. TEM image showing an overview of the 100 dpa sample. Enhanced image in the red box shows near-surface region of the Zr_3Fe phase.

precipitates in the peak ion range, consistent with the precipitation seen in Figure 18a and Figure 18b.

Figure 20a shows a TEM image of the $FeZr_3$ region of the 100 dpa sample. Figure 20b and Figure 20c are enlarged images of the $FeZr_3$ near-surface, showing the formation of irradiation-induced precipitation. Figure 20d is an indexed Fast Fourier Transform (FFT) taken from this region, confirming it is $FeZr_3$ and not $(Fe,Cr)_2Zr$. Near-surface precipitation occurred in $FeZr_3$ in all three irradiation conditions. The zoomed-in TEM image in the red box of Figure 21 shows the Zr_3Fe region away from the amorphous region. The near-surface region is still clear of voids, indicating that void formation in the near-surface region shown in Figure 20b and Figure 20c was not simply suppressed by the nearby amorphous region. Another example is found in the near-surface region of the 50 dpa sample, shown in Figure 22a. Figure 22b is an enlarged, under-focused image

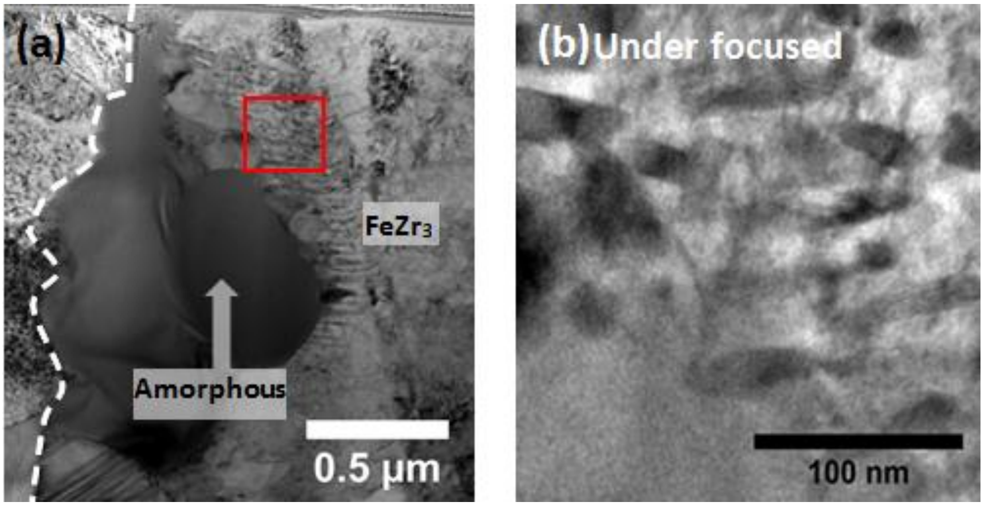

Figure 22. (a) TEM image of the near-surface region of $FeZr_3$ from the 50 dpa sample. (b) Enlarged image from the red box in (a).

from the red box area of Figure 22a, and shows the precipitation in more detail. A likely mechanism for the formation of these laminar precipitates is decomposition of $FeZr_3$. It is generally accepted that $FeZr_3$ is stable up to a temperature very close to the liquidus line of the Fe-Zr system, but there is a temperature region in which $FeZr_3$ disappears and dissolves into $FeZr_2$ and β-Zr [20]. Under ion irradiation involving thermal spike formation, peritectoid dissolution may occur due to rapid quenching. No white dots are visible in Figure 22b, suggesting the lack of void formation and swelling.

3. Ti_2AlC-COATED ZIRCALOY-4*

MAX phase materials are particularly attractive because their unique layered structure provides the benefits of both ceramics and metals with fewer drawbacks. ‘MAX’ refers to the layered structure of ‘M,’ an early transition metal (Ti, Mo, Cr, Zr, Nb), an ‘A’group element (Al, Si, Ga, Sn, Pb), and an ‘X’ group element (C or N). With the correct contents of its A and X group elements, this layered structure provides the ability of the MAX phase to conduct heat and electricity similar to metal, but resist oxidation similar to ceramics, and has a promising application as a nuclear fuel cladding or coating [43]. Figure 23 shows the crystal structure of MAX Phase materials [44]. Ti_2AlC in particular satisfies the strength, ductility, melting point, and heat transfer characteristics necessary to act as a coating or cladding. It is a 211 MAX Phase, and therefore possesses the crystal structure noted in Figure 23a.

However, as with FeCrAl, consideration must be given to core neutronics. The ‘M’ group of the MAX phase is what dominates the thermal neutron absorption cross section, and in the case of Ti_2AlC, the cross-section is dominated by natural titanium,

---

* A part of this chapter is reprinted with permission from M. W. Barsoum and M. Radovic, "Elastic and Mechanical Properties of the MAX Phases," Annual Review of Materials Research, vol. 41, pp. 195-227, 2011, Copyright 2020 by Annual Reviews.

A part of this chapter is reprinted with permission from J. G. Gigax, M. D. Kennas, H. Kim, T. Wang, Maier, B. R., H. Yeom, G. O. Johnson, K. Sridharan and L. Shao, "Radiation Response of Ti2AlC MAX phase coated Zircaloy-4 for accident tolerant fuel cladding," Journal of Nuclear Materials, vol. 523, pp. 26-32, 2019, Copyright 2020 by Elsevier.

A part of this chapter is adapted with permission from C. Li, J. She, M. Pang and W. Yang, "Phase Equilibria in the Al-Zr-Nd System at 773 K," Journal of Phase Equilibria and Diffusion, vol. 32, pp. 24-29, 2011, Copyright 2020 by Elsevier.

whose cross-section is 8.3 barns [45]. Neutronics analysis of this particular MAX phase shows that if the coating is kept to approximately 25 µm or less, the neutron economy of the reactor is not significantly impaired [6].

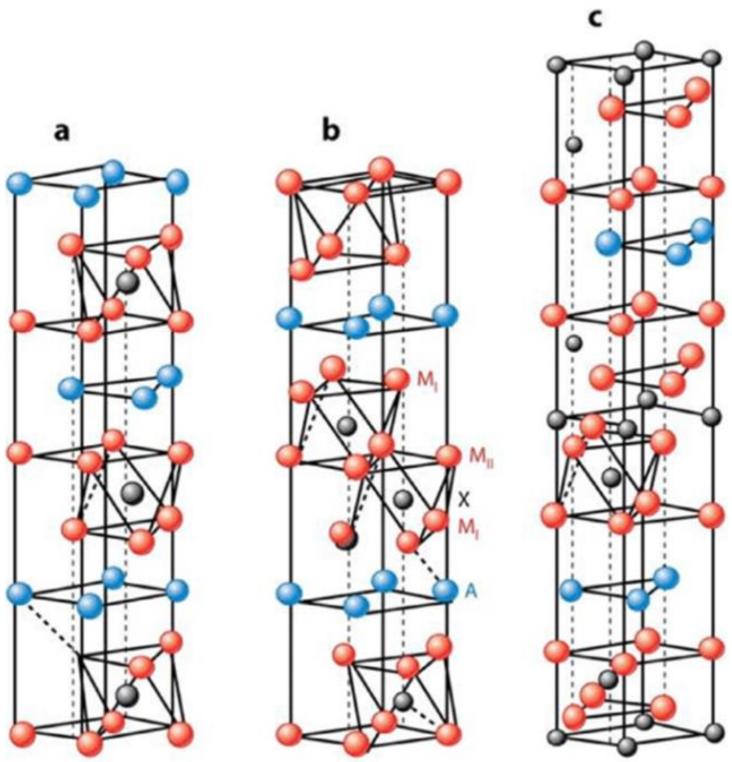

Figure 23. MAX Phase crystal structure of (a) 211, (b) 312, and (c) 413 phases. Red atoms are the 'M' component, blue are the 'A' component, and black are the 'X' component. Reprinted with perission from [44] Copyright 2020 by Annual Reviews.

3.1 Experimental Procedure

The experimental procedure for the TiAlC-coated Zircaloy-4 samples is similar to the procedure of the FeCrAl-coated Zircaloy-4 samples. Zircaloy-4 bulk was coated with Ti_2AlC by UWM using the cold-spray process [7] outlined in Section 2, Subsection 2.1.

The received coated bulk was cut into 3x3x3mm individual samples via a SiC cutting blade. These samples were sealed inside a quartz tube with an inner volume evacuated to $1x10^{-6}$ torr. The sealed, evacuated tube was placed in a furnace; the sample intended for ion implantation was annealed at 923 K for 314 hours, as this provided the thickest cross-sectional interface for the irradiation. Samples intended for diffusion kinetics analysis were annealed at 873 K and 898 K for 168 hours, and 923 K for 168 and 314 hours, respectively. All samples were heated and cooled at a rate of 10 °C/min. These temperatures were selected to promote the most rapid interdiffusion while avoiding the typical melting point of aluminum at 933 K.

Following annealing, samples were extracted and mechanically polished along the cross-sectional face using 1200 grit SiC abrasive papers, then fine polished with a 0.25 µm alcohol-based diamond solution. As with the FeCrAl-coated samples, the final alcohol-based solution was selected because analyses of these samples do not require ultra-fine (~0.05 µm) polishing, and this solution is not water-based, in order to resist oxidizing the polished Zircaloy-4 surface for as long as possible.

Micromechanical testing to study the mechanical properties of the intermetallic phases was performed using a Hysitron TI950 Triboindenter equipped with a Berkovich tip for nanoindentation. Samples were all loaded to a maximum force of 2.5 mN.

SEM images were obtained from a FEI Quanta 600 scanning electron microscope equipped with BSED and EDS detectors. TEM microscopy was performed using a FEI Tecnai F20 transmission electron microscope equipped with a high angle annular dark field (HAADF) detector. A TESCAN LYRA-3 gallium FIB was used to fabricate 100 nm-thick TEM lift-outs.

Ion irradiation was performed using a 1.7 MV Ionex Tandetron ion accelerator. Ion bombardment was targeted towards the cross-sectional face and used Zr^{2+} ions accelerated to 3.5 MeV. Zr ions were selected in favor to Al ions as aluminum diffusion into zirconium was predicted through diffusion kinetics calculations, while Zr diffusion is once again largely negligible. The sample was irradiated at 723 K to 100 peak dpa using 3.5 MeV Zr^{2+} ions. A static, defocused beam with a nominal dose rate of 2.34×10^{-3} dpa/s was maintained within ±5%. SRIM predicted the upper range of 3.5 MeV Zr^{2+} ions to be approximately 1.3 µm in TiAlC and 1.0 µm in Zircaloy-4 [17].

3.2 Intermetallic Formation

Figure 24a shows a SEM image of the cross-sectional face of the virgin sample. Consistent with the FeCrAl-coated samples, the cold-spray process introduced a mild amount of interdiffusion between the coating and substrate [46]. Figure 24b and Figure

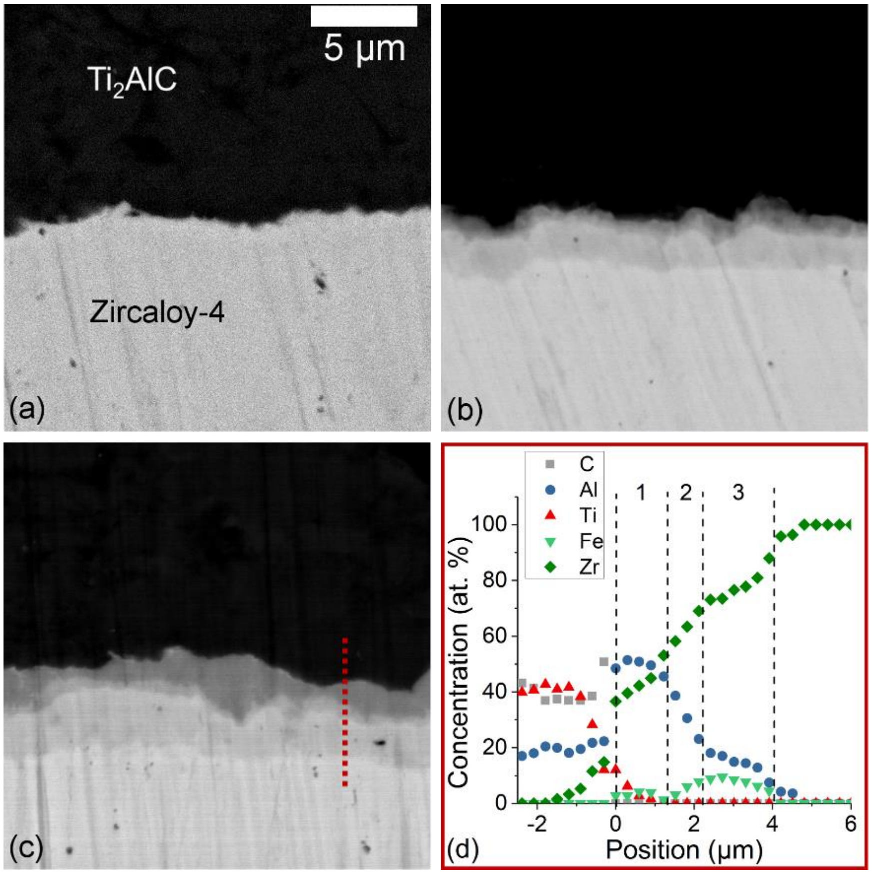

Figure 24. SEM images of the (a) as-received Ti2AlC coated Zircaloy-4 specimen, the specimen annealed at 923 K for (b) 168 hours, and (c) 314 hours. An EDS line scan, shown in (c) by a dotted red line, is given in (d). Reprinted with perission from [46] Copyright 2020 by Elsevier.

24c show the interface zones of the TiAlC coated sample, and Figure 24d shows EDS data of the interface zone of the sample annealed at 923 K for 314 hours.

Only two intermetallic phases were observed in the sample annealed for 168 hours. After an additional 168 hours, the intermetallic phases observed in the 168 hours sample grew, and an additional phase appeared. The EDS data of Figure 24d confirm the existence of three intermetallic phases between the substrate and coating. EDS point scans across this interface region identified the intermetallics, in order between TiAlC and Zircaloy-4, as $ZrAl_2$, ZrAl, and Zr_3Al, respectively. This is consistent with phases shown to form in the binary Zr-Al phase diagram [47]. Figure 26 shows a STEM

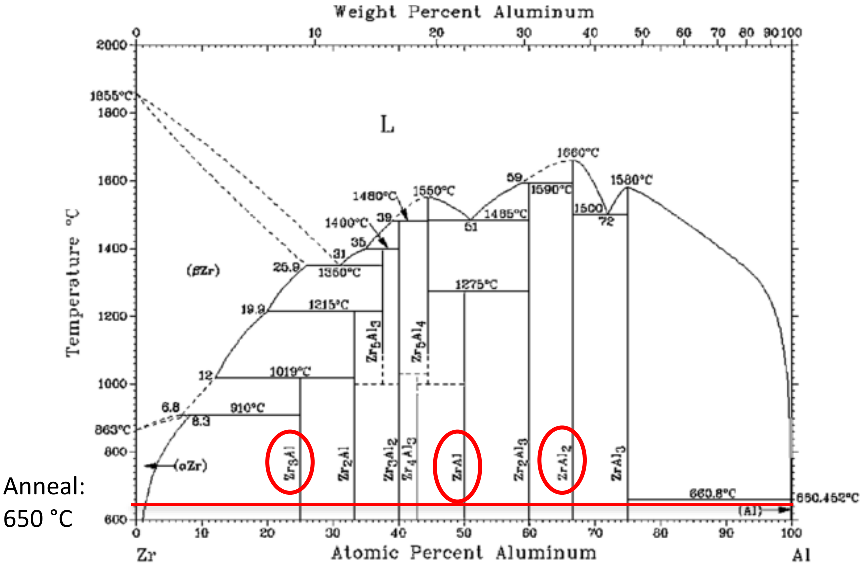

Figure 25. Binary phase diagram of the Zr-Al system. The red line indicates highest annealing temperature. The circled phases were observed in the TiAlC-coated samples following annealing Adapted with permission from [47] Copyright 2020 by Elsevier.

micrograph taken via HAADF detector of the interface zone and an EDS line scan across the interface. The line scan shows three distinct signals between TiAlC and Zircaloy-4, in agreement with the line scans shown in Figure 24. Data from EDS point scans used to positively identify the compositions of the intermetallics are shown in Table 3.

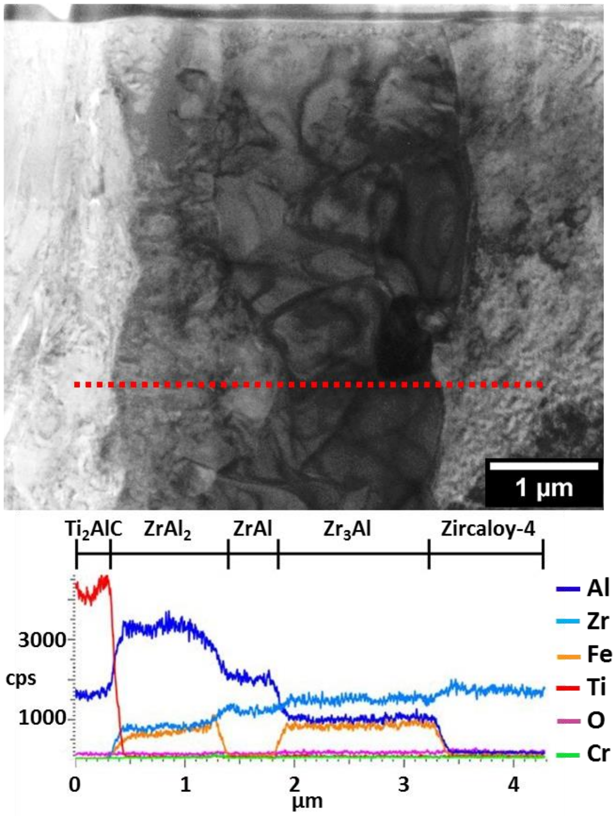

Figure 26. HAADF STEM image of the interface zone between TiAlC and Zircaloy-4 following 314 hours of annealing at 923 K. Reprinted with perission from [46] Copyright 2020 by Elsevier.

Table 3. Atomic compositions and average thicknesses of the intermetallics in the TiAlC-coated sample annealed at 923 K for 314 hours.

Compound	**Zr (at %)**	**Ti (at %)**	**Al (at %)**	**C (at %)**	**Fe (at %)**	**Sn (at %)**	**Thickness (μm)**
Ti_2AlC	0	34.6	22.9	42.4	0.1	0.0	--
Al_2Zr	39.8	0.2	56.7	0.0	2.9	0.4	1.52
ZrAl	53.8	0.0	44.7	0.0	0.6	0.9	0.53
Zr_3Al	66.1	0.0	20.8	0.0	11.8	1.3	2.37
Zircaloy-4	98.2	0.0	0.0	0.0	0.6	1.3	--

3.3 Diffusion Kinetics

Figure 27a-d show comparisons of the growth of intermetallics between TiAlC and Zircaloy-4 over different annealing temperatures and durations. Two intermetallics ($ZrAl_2$ and Zr_3Al) developed relatively early, with a third (ZrAl) following at the highest annealing time and temperature. This delayed appearance of ZrAl indicates that it is the least thermodynamically favorable of the three phases observed in this system to develop.

As predicted, Al diffusion dominated the interdiffusion regime, owing to its high diffusivity from TiAlC [48]. EDS line and point scan data from Figure 26 and Table 3 indicate the presence of some Fe and Ti diffusion in the interface zone, but Al diffusion is what dictated the formation of intermetallic compounds and their relative thicknesses. Diffusion kinetics of the Al into Zircaloy-4 can be estimated by measuring the phase widths normalized to annealing time and plotting against temperature. Figure 27e shows the results of this plot. From this, the activation energy of the Al diffusion was calculated to be approximately 202 kJ/mol [46]. When comparing to the activation energy of 180 kJ/mol reported from previous studies on Al-Zr diffusion couples [49, 50, 51], the activation energy of this system is somewhat elevated. There are two likely explanations for this: in TiAlC, Al is not present as a single element as part of a uniform bulk matrix. Instead, it is present as a nanolaminate layer sandwiched between TiC layers of the MAX phase structure of Ti_2AlC [52]. As a result, Al diffusion is dependent largely on grain orientation at the virgin interface. The second reason is that there may be discontinuities

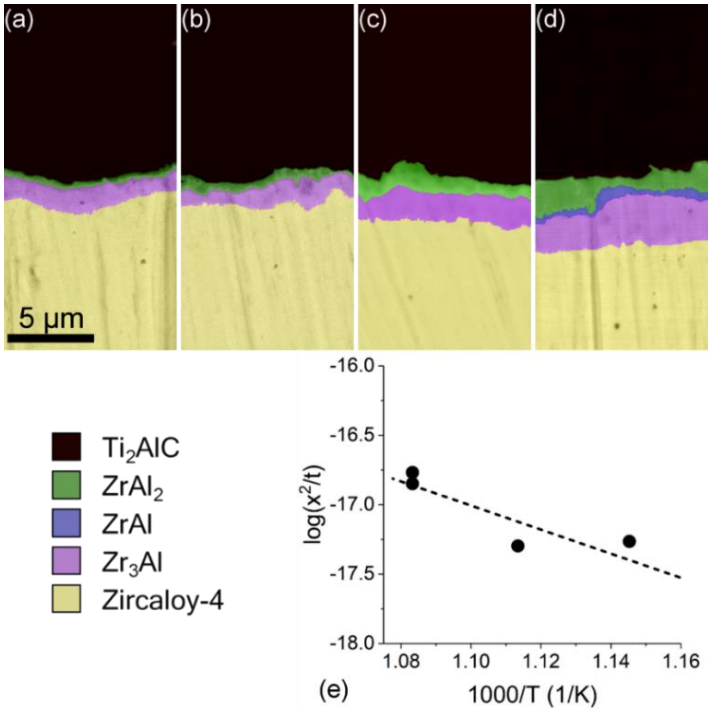

Figure 27. SEM images of Ti_2AlC coated Zircaloy-4 annealed at (a) 873 K, (b) 898 K, and 923 K for (c) 168 hours, and (d) 923K for 314 hours, respectively. The diffusion width, x, normalized to annealing time, t, as a function of reciprocal temperature is given in (e). Reprinted with perission from [46] Copyright 2020 by Elsevier.

between the TiAlC cold-sprayed coating and Zircaloy-4 substrate, including broken up oxides on the surface of the Zircaloy-4 and porosity of the coating as mentioned in Section 2, Subsection 2.3. The combination of these factors would increase the difficulty for Al to diffuse into Zircaloy-4, resulting in the higher apparent activation energy.

3.4 Irradiation Response of Coating and Intermetallics

For the purpose of this research, TEM was utilized to observe the changes to the microstructures of the intermetallic regions after ion irradiation. Figure 28 shows the TiAlC-Zircaloy-4 interfacial zone following 314 hours of implantation at 923 K and 100

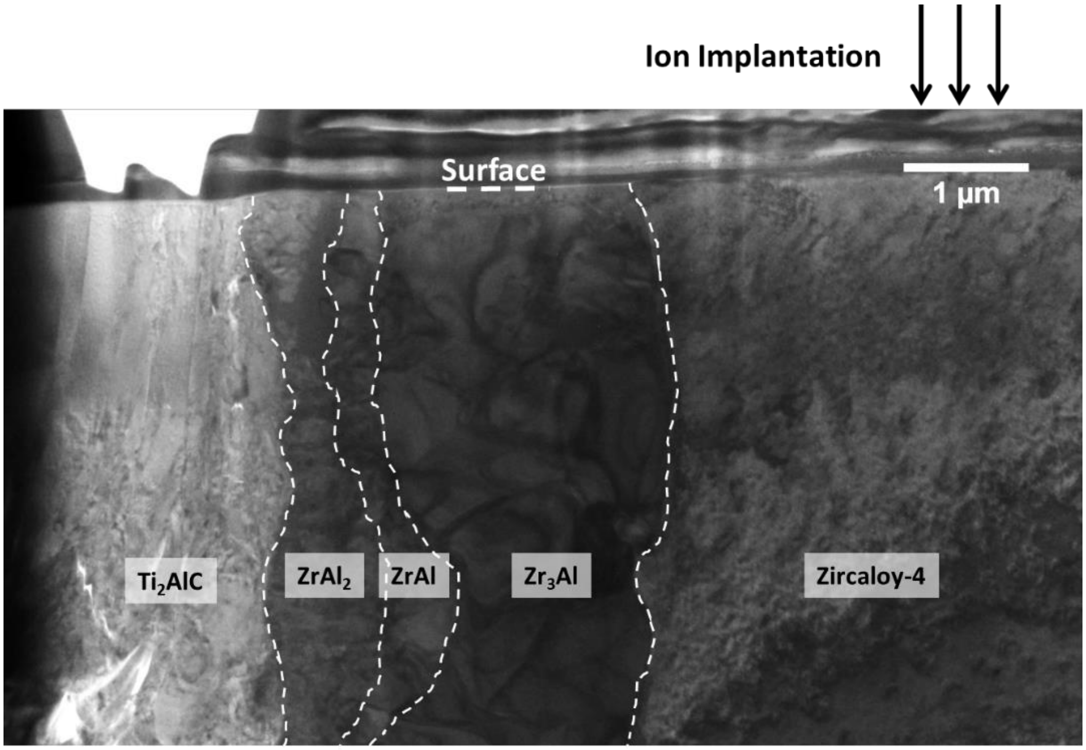

Figure 28. STEM HAADF micrograph of the full TiAlC-Zircaloy-4 interfacial zone following 314 hours of implantation at 923 K and 100 peak dpa ion implantation. The surface and ion implantation direction are marked.

peak dpa ion implantation. The image has been segmented to add ease of identification of the intermetallics. EDS line scan data from Figure 26 was used to discern phase

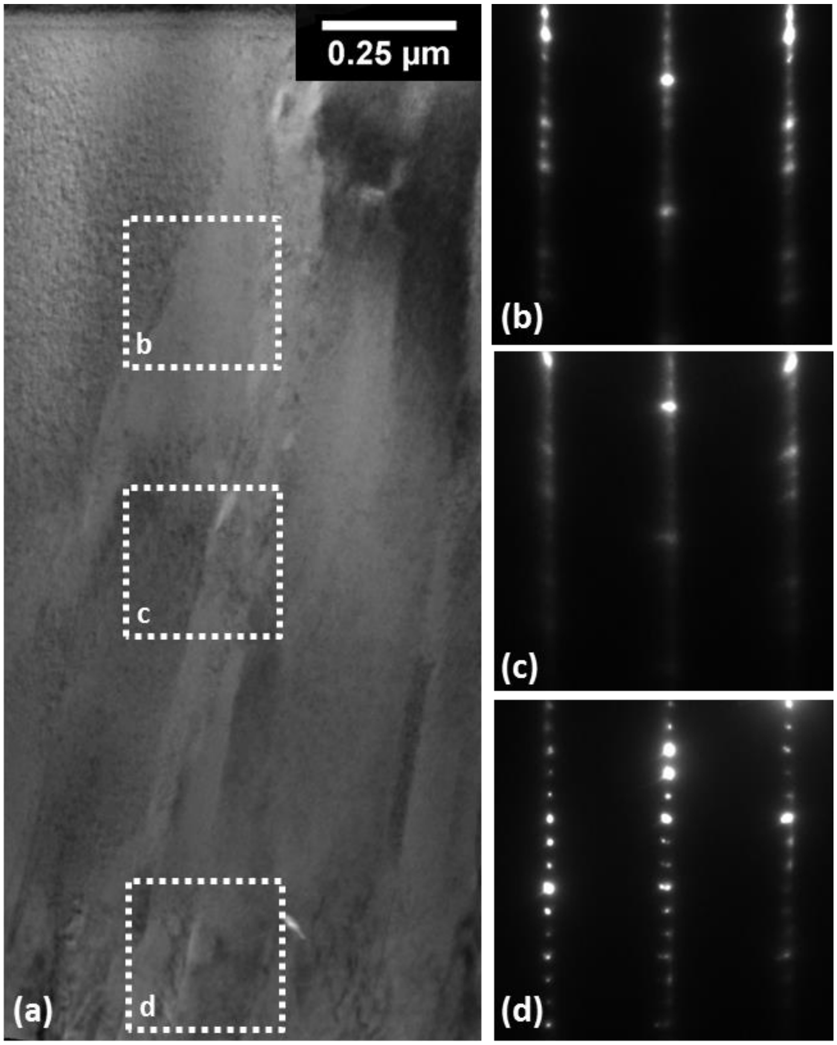

Figure 29. (a) Bright field TEM image of TiAlC coating near the interface with diffraction patterns at depths (b) within the ion penetration range, (c) peak damage region, and (d) beyond the ion penetration range. Reprinted with perission from [46] Copyright 2020 by Elsevier.

boundaries. Note the porosity visible towards the bottom of the TiAlC coating in the image.

Figure 29a shows a TEM image of the TiAlC coating near the interphase region following 100dpa ion implantation. SRIM predicted the ion peak implantation range into

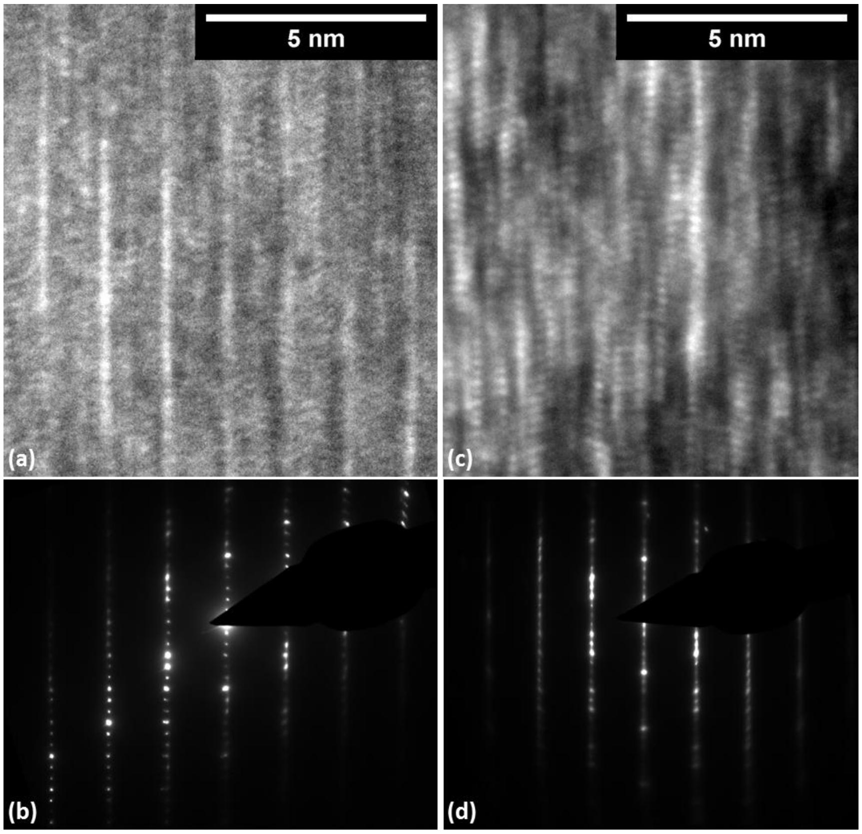

Figure 30. (a) HRTEM micrograph of TiAlC beyond ion penetration range (at 1900nm), with diffraction pattern (b) taken in this region. (c) HRTEM of TiAlC within ion penetration range (at 500nm), and diffraction pattern (d) taken within this region Reprinted with perission from [46] Copyright 2020 by Elsevier.

the TiAlC coating as approximately 1.3 µm [17]. To compare radiation effects against unirradiated TiAlC, diffraction patterns of the coating within ion penetration range (500nm), peak damage (1000nm), and beyond ion range (1900nm), were extracted. These diffraction patterns are shown in Figure 29b, c, and d, respectively [46]. At the 500nm depth, corresponding to roughly 50 dpa, the spots of the diffraction pattern appear distinct against a relatively diffuse background. At 1000nm, corresponding to roughly 100 dpa, the spots are fainter and the background is significantly more diffuse, but there are no strong halo features indicative of amorphization. Instead, these diffuse spots are indicative of high dislocation or stacking fault densities. At 1900nm, beyond ion penetration range, the spots are clear and mildly diffuse, likely resulting from defects introduced by FIB [53].

The HRTEM and diffraction patterns shown in Figure 30 were also taken from the TiAlC coating. Figure 30a and Figure 30b were taken beyond the ion penetration range. Microstructure ordering is good, and the diffraction pattern shows no indication of diffuse regions. From Figure 30a, the spacing of the Al layers was measured to be approximately 1.36 nm, consistent with literature on this particular MAX phase [52]. From the diffraction pattern of Figure 30b, the lattice parameters were calculated to be a = 0.3 n, and c = 1.36 nm [46]. Comparing Figure 30a to Figure 30c, it is clear that the irradiated TiAlC still shows some of the nanolaminar structure expected of MAX phases. However, there clearly is heavy disordering of the crystal structure. Figure 29b and Figure 29c show the average lattice spacing in the $[11\bar{2}0]$ direction did not increase after further irradiation damage, despite the HRTEM image of Figure 30c showing disordering of the layers along the [0001] direction. The diffraction pattern shown in Figure 30d once

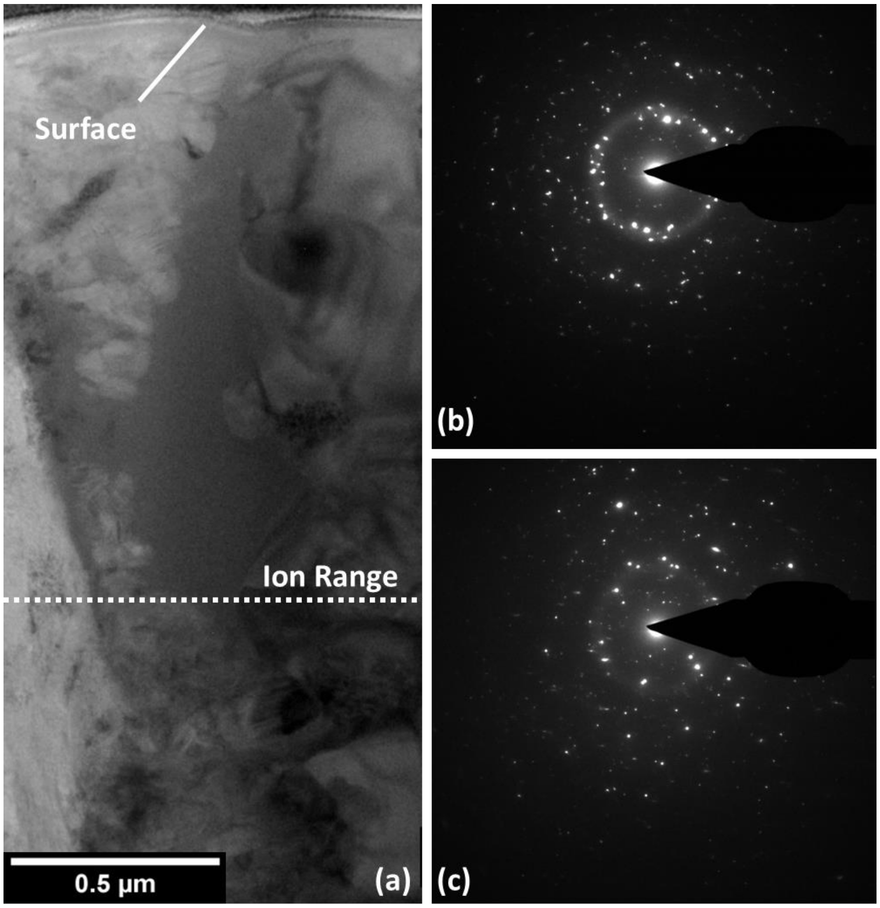

Figure 31. (a) Bright field TEM image of $ZrAl_2$ and ZrAl. (b) Diffraction pattern extracted within the ion penetration range and outside the amorphized region. (c) Diffraction pattern taken from outside the ion penetration range. Reprinted with perission from [46]. Copyright 2020 by Elsevier.

again indicates diffuse regions between the spots, consistent with the diffuse diffraction patterns of Figure 29b and Figure 29c and reflective of the irradiation damage introduced to this region.

Figure 31a shows a bright field image of the $ZrAl_2$ and ZrAl region. The expected maximum ion penetration range of this region simulated by SRIM is approximately 1.3 µm [17]. Both $ZrAl_2$ and ZrAl have an orthorhombic crystal structure [54, 55], but the diffraction patterns in both Figure 31b and Figure 31c show a polycrystalline signal. This is attributed to the fine grain overlap of this region, as both intermetallics are expected to have a grain size finer than the width of the TEM lamella. To be discussed later in this section, it may also be attributed to small concentrations of the intermetallics Zr_4Al_3, Zr_2Al_3, and $ZrAl_3$. It is noted that the diffraction pattern in Figure 31b shows a prominent amorphous ring, despite being taken from outside of the amorphous region visible in Figure 31a. This indicates partial amorphization of the $ZrAl_2$ and ZrAl region. The diffraction pattern in Figure 31c also shows an amorphous ring, despite being taken from

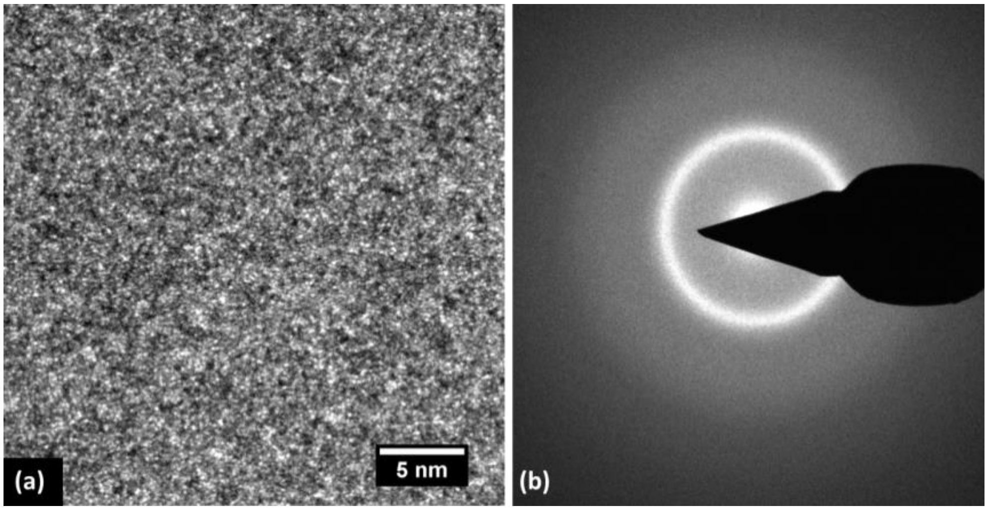

Figure 32. (a) HRTEM of the amorphous region between $ZrAl_2$ and ZrAl. (b) Diffraction pattern taken from this amorphous region. Reprinted with perission from [46] Copyright 2020 by Elsevier.

beyond ion penetration depth, indicating mild temperature-induced amorphization of this region. This amorphization is exacerbated and stabilized by the melting and subsequent quenching induced by the irradiation [37, 38], resulting in the more prominent diffuse signal in Figure 31b. Comparing Figure 31c to Figure 30d, it is evident that under irradiation this region better retained its nanocrystalline structure when compared to the response of TiAlC.

It should be noted that because TEM offers higher resolution when compared to SEM, closer observation made it less certain if ZrAl is the only phase present in the area with $ZrAl_2$. The phase diagram in Figure 25 indicated the potential existence of Zr_4Al_3, Zr_2Al_3, and $ZrAl_3$ given the annealing conditions. Given the narrow phase widths and small grain sizes coupled with the relatively coarse nature of EDS scanning, it is possible that these intermetallics may exist in relatively small concentrations and they are difficult to positively identify. However, the region presents as a single signal in the EDS line scan from Figure 26, and from point scans it matches the general atomic stoichiometry of ZrAl (Table 3), and thus will be referred to as such.

The amorphous region visible in Figure 31a extends to the maximum depth of ion irradiation. Confirmation of full amorphization is given by the lack of crystalline structure visible in the HRTEM image shown in Figure 32a and full diffuse ring in the diffraction pattern shown in Figure 32b. EDS point scans of the amorphous region match its composition to $ZrAl_2$, however positive identification is challenged by the thin width of the $ZrAl_2$/ ZrAl region versus the coarse size of the EDS point scan. Further testing may be necessary to positively confirm if it is $ZrAl_2$, ZrAl, or one of the smaller Zr_4Al_3, Zr_2Al_3, or $ZrAl_3$ intermetallics that amorphized. It is noted that amorphization did not engulf the entire $ZrAl_2$/ ZrAl region. High irradiation temperature and the presence of grain boundaries at the interface between $ZrAl_2$ and TiAlC both helped to facilitate defect recombination and removal, resulting in incomplete amorphization near the interface and sample surface.

Figure 33a shows a TEM image of the near-surface region of the Zr_3Al intermetallic phase. Within ion irradiation, there is a visibly higher density of dislocation loops visible than below ion penetration range. Though lifting out of a TEM lamella via FIB has been known to be a cause of dislocations [53], there is a distinct lower density visible below ion penetration range, indicating that ion irradiation induced higher dislocation density into the material beyond that of FIB-induced damage. Comparing the lattice structures visible in Figure 33b and Figure 33c shows the lattice disordering introduced by the irradiation, though the effect is less severe than that seen in TiAlC.

Visible in Figure 33a is the amorphous precipitate $Zr(Fe,Cr)_2$ [46]. The diffraction pattern in Figure 33d was taken from this precipitate, and it shows a bright diffuse signal along with a lack of discernible spots, indicating complete amorphization. From Section 2, Subsection 2.4, this material was noted to be present as an intermetallic between FeCrAl and Zircaloy-4, and like what is observed here in Zr_3Al, was shown to be amorphized under irradiation [21].

The growth of $Zr(Fe,Cr)_2$ precipitates in Zr_3Al can be attributed to sufficient Al diffusion into Zircaloy-4 coupled with energetically favored formation of $Zr(Fe,Cr)_2$ in Zircaloy-4. The low concentrations of Fe in Zircaloy-4 limit the growth of $Zr(Fe,Cr)_2$ to precipitates, whereas in the case of the FeCrAl-coated zircaloy-4 samples, sufficient Fe diffusion from the FeCrAl coating allowed for $Zr(Fe,Cr)_2$ to form as a complete intermetallic layer. In this case, isolated pockets of $Zr(Fe,Cr)_2$ formed simultaneously with Zr_3Al, resulting in the $Zr(Fe,Cr)_2$ precipitates.

The diffraction pattern of Figure 34a, in which dots from the crystalline structure and a diffuse amorphous ring are visible, indicates that partial amorphization in the near-surface, ion irradiated region of Zr_3Al has occurred. An HRTEM image, shown in Figure 34b, taken from the same region reflects this. Regions of ordered crystal lattice are visible

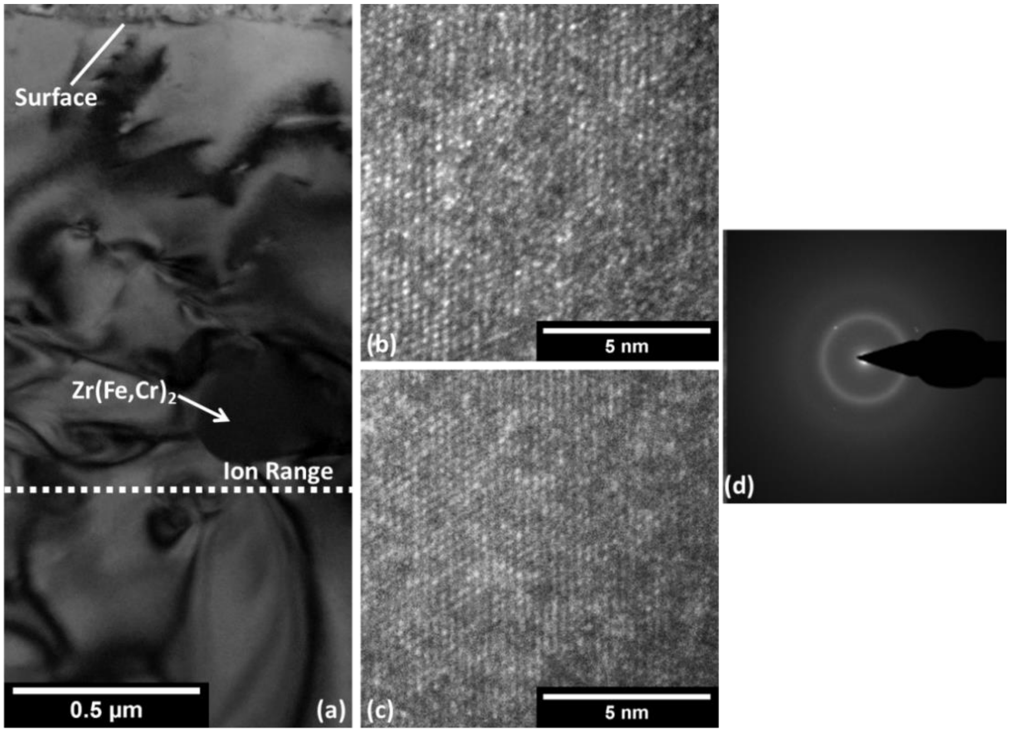

Figure 33. (a) TEM image of the Zr_3Al intermetallic. (b) HRTEM image taken in the near-surface region of (a). (c) HRTEM image taken beyond ion penetration range. (d) Diffraction pattern of the $Zr(Fe,Cr)_2$ precipitate in (a). Reprinted with perission from [46] Copyright 2020 by Elsevier.

in the upper left corner and towards the edges of the figure, while a disordered amorphous region is visible towards the center. Studies have shown that zirconium-based intermetallics such as Zr_3Al can amorphize over a wide range of irradiation parameters [56, 57]. In order for amorphization of the intermetallic to occur, defect buildup and irradiation-induced disorder must result in the free energy difference of the non-irradiated and irradiated system to exceed the free energy difference of the crystalline and amorphous phase [34]. Additionally, the effect of deposited energy density and dose rates must be considered in the formation of amorphous materials. High dose rates result in enhanced beam mixing of the irradiated region, leading to higher rates of defect recombination, therefore requiring higher doses to achieve amorphization. However, a lower dose is needed for heavy ion irradiation in comparison to low deposited energy irradiations such as e^- irradiations. In this case, a high dose (100 peak dpa) combined with

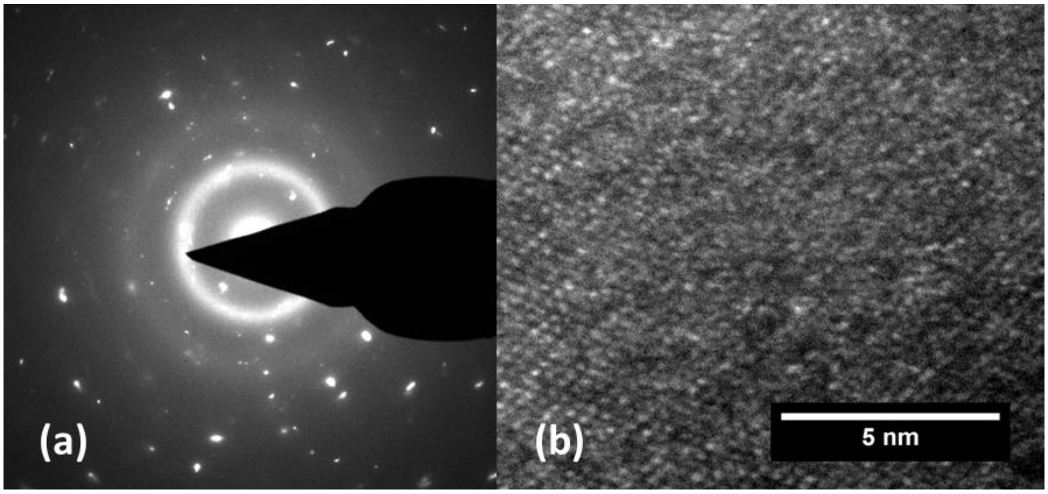

Figure 34. (a) Diffraction pattern of near-surface region of Zr_3Al. (b) HRTEM of the same region as (a).

high dose rate (2.34 x 10^{-3} dpa/s) resulted in amorphization of the zirconium-based intermetallics [46].

To gauge the material properties change of the intermetallics and coating after irradiation, nanoindentation was performed along the cross section of the 923 k, 314 hour sample to obtain hardness measurements of each phase. The load-displacement curves of TiAlC before and after irradiation are shown in Figure 35a, and hardness values of TiAlC, $ZrAl_2$, Zr_3Al, and Zircaloy-4 before and after irradiation are shown in Figure 35b. ZrAl nanoindentation data is unavailable due to its narrow average phase width, and will be treated as being a part of the $ZrAl_2$ data.

The hardness of TiAlC was observed to increase by approximately 140% following irradiation [46]. This behavior is noted to be consistent with a similar 2-1-1 MAX phase, Cr_2AlC [32]. This hardening is likely the result of an increased density of dislocation loops in the near-surface region. Zircaloy-4 hardness was found to have increased by 164% [46]. As with the TiAlC, this is attributed to the increase in dislocation loop density as a result of irradiation damage in the near surface region.

The increase in hardness for Zr3Al was measured to be 140% [46]. This hardness change is not necessarily the result of a single mechanism. Previous studies [58, 59, 60] into irradiation damage of Zr_3Al indicated increased strength and reduction in ductility, owing to the irradiation-induced increase in dislocation loops and the development of hardened amorphous $Zr(Fe,Cr)_2$ in the near surface region.

The ZrAl/ $ZrAl_2$ phase was the only one in which a significant change in hardness was not observed [46]. The small grains of this phase resulted in an increase in the density of grain boundaries, which acted as defect sinks that helped to counteract the increase in dislocation density seen in the other phases. Additionally, the lack of hardness change suggests that the mixed amorphous/ nanocrystalline region does not provide significant strengthening or weakening over a nanocrystalline microstructure alone, though it is noted the nanoindentation testing was performed at room temperature. Therefore, it is currently unclear if the elevated temperatures of routine core operation or a LOCA will impact the strength of this phase.

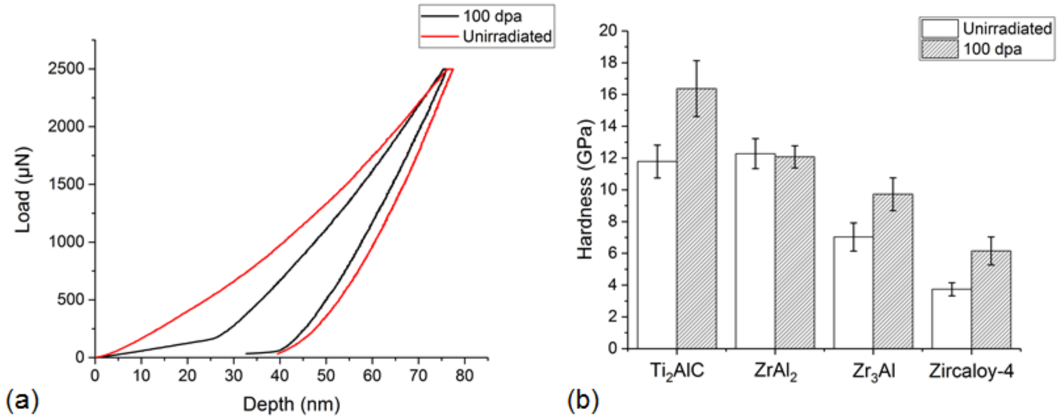

Figure 35. (a) Load-displacement curves of TiAlC before and after 100 peak dpa irradiation. (b) Hardness values of TiAlC, $ZrAl_2$, Zr_3Al, and Zircaloy-4. AFM image of selected indents shown above (b). Reprinted with perission from [46] Copyright 2020 by Elsevier.

4. PURE CHROMIUM-COATED ZIRCALOY-4[*]

Pure chromium has been considered as a potential cladding coating material due to its extraordinary corrosion resistance, high strength, hardness, wear resistance, and high melting point [61]. Additionally, it has a very low neutron absorption cross-section relative to other naturally-occurring elements, at 0.76 barns [45].

There is already experience with chromium inside reactor cores, as control rods in some LWRs are plated with chromium to increase wear resistance; chromium is also typically present in reactor cores as an alloying element in structural steels [61].

Micromechanical properties testing had already been conducted on irradiated vs unirradiated pure Cr during a related study. The pure Cr was irradiated to 50, 100 and 150 dpa with 5 MeV Fe^{2+} ions at a stage temperature of 550 °C using a 3MV NEC Pelletron ion accelerator. The findings, shown in Figure 36a and Figure 36b, indicate that the ductility of pure Cr decreases with relatively low dose, then proceeds to increase with higher doses. The hardness doubles at 50 dpa and saturates from there. These are consistent with findings showing that hardness increases in pure Cr with high amounts of mechanical damage [62]. These results indicate that damage induced via ion irradiation

---

[*] Part of this chapter is adapted with permission from H. J. Lu, W. B. Wang, N. Zou, J. Y. Shen, X. G. Lu and Y. L. He, "Thermodynamic Modeling of Cr-Nb and Zr-Cr with Extension to the Ternary Zr-Nb-Cr System," CALPHAD, vol. 50, pp. 134-143, 2015, Copyright 2020 by Elsevier.

Part of this chapter is reprinted under open access from Z. Zhang, D. Balint and F. Dunne, "Rate sensitivity in discrete dislocation plasticity in hexagonal close-packed crystals," Acta Mater., vol. 107, pp. 17-26, 2016, Copyright 2016 by Elsevier.

provides similar mechanical properties changes to mechanically induced plastic deformation.

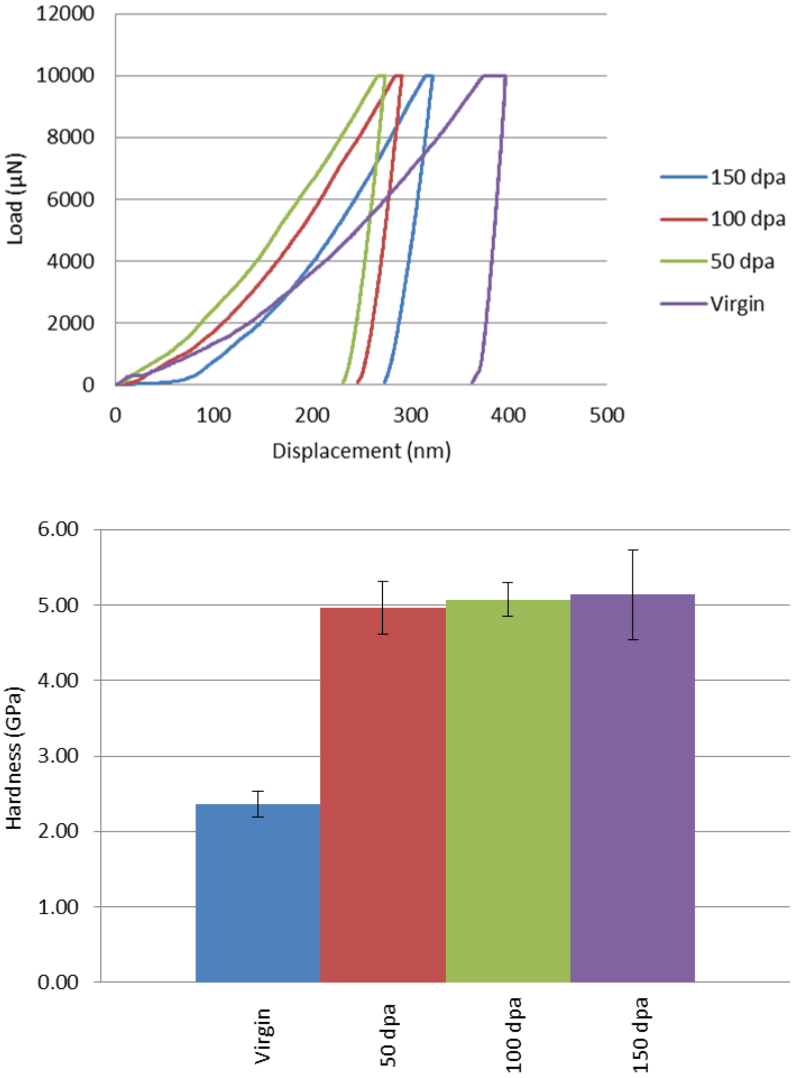

Figure 36. (a) Load-displacement curves for unirradiated pure Cr and pure Cr irradiated to 50, 100, and 150 dpa. (b) Corresponding hardness values.

4.1 Evaluating Experimental Procedures

As was the case for the FeCrAl and TiAlC coatings, pure Cr was cold-sprayed by UWM onto Zircaloy-4 that had been polished with 320-grit SiC paper [7]. One notable difference in this case was that the average thickness of the Cr coating was approximately 12 µm thick on average, versus the 100-150 µm thickness of FeCrAl and TiAlC.

The received coated bulk was cut into 3x3x3mm individual samples via a SiC cutting blade. These samples were sealed inside a quartz tube with an inner volume evacuated to 1x10^{-6} torr. The sealed, evacuated tube was placed in a furnace and the samples were annealed at 998 K for 504 hours, then annealed again at 998 K for an additional 504 hours, for a final anneal duration of 1008 hours. All samples were heated

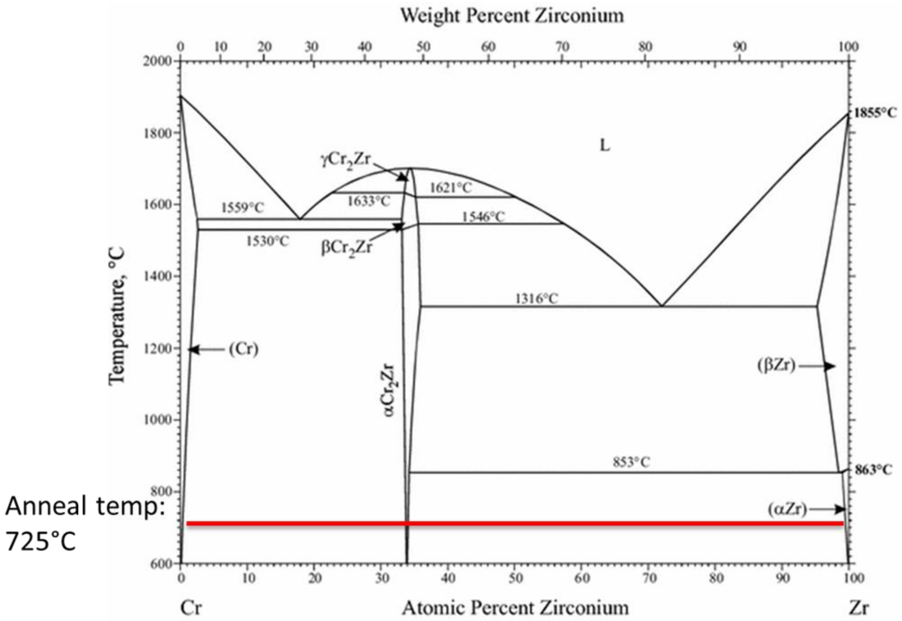

Figure 37. Phase diagram of the Zr-Cr system. Annealing temperature of 725 °C indicated by the red line. Adapted with permission from [63] Copyright 2020 by Elsevier.

and cooled at a rate of 10 °C/min. These temperatures were selected to promote the most rapid interdiffusion while avoiding the phase transition of the zirconium from α-Zr to β-Zr seen in Figure 37.

Following annealing samples were cut and mechanically polished along the cross-sectional face with 4000-grit SiC paper, followed by the same 0.25 µm alcohol-based polycrystalline diamond solution used in Section 2, Subsection 2.1 and Section 3, Subsection 3.1 for the FeCrAl-coated samples and TiAlC-coated samples. This stage of polishing was found to be too coarse for the use of EBSD, even after Xe beam etching

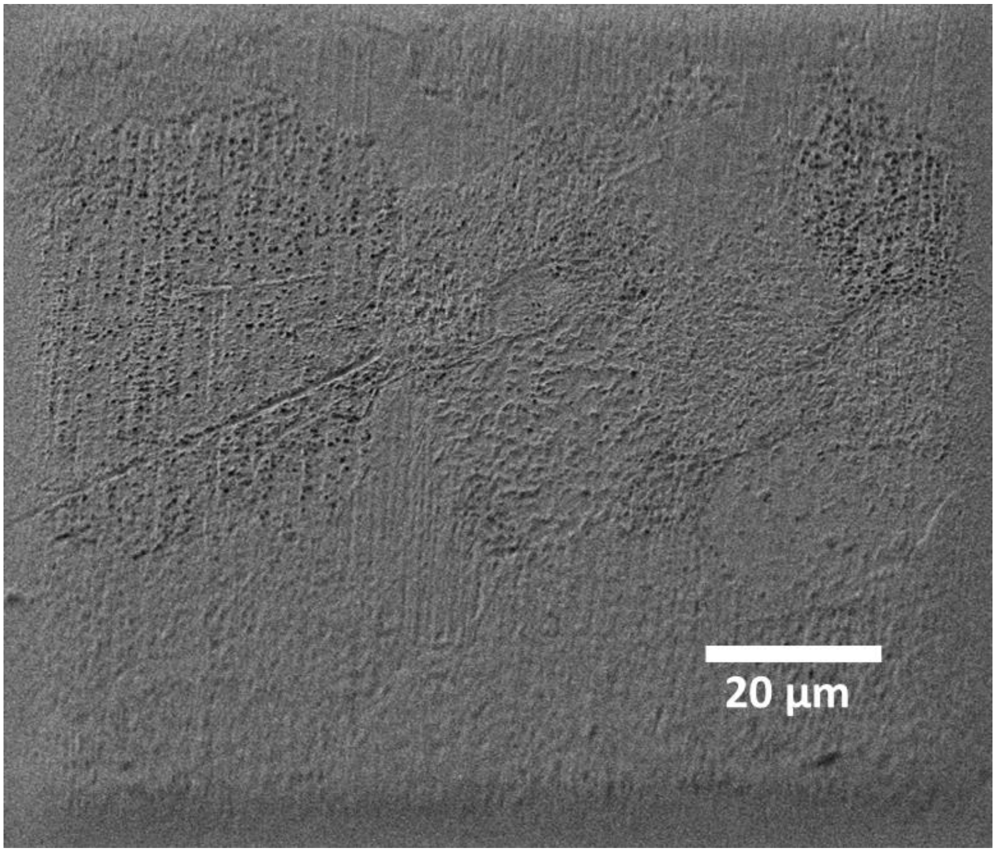

Figure 38. SEM image of Cr-Zircaloy-4 interface region following 0.25 um solution polishing and Xe beam etching.

away of a 100 nm-thick surface region, with the intent of removing oxidation and surface imperfection (Figure 38). Finer polishing was required; the 0.25 µm alcohol-based polycrystalline diamond solution step was then followed by a supplementary 0.04 µm glycol-based polycrystalline diamond solution step. This solution still proved to be insufficient for EBSD, necessitating 100nm surface etching via Xe ion beam (Figure 39). This proved to be sufficient for EBSD, however, the propensity of Zircaloy-4 to strongly oxidize limited the usable timeframe of these ultra-fine polished samples to only several days, challenging many later attempts at EBSD due to the oxide layer formed at the Cr-Zircaloy-4 interface.

Scanning electron microscopy (SEM) imaging was performed using a FEI Quanta 600 scanning electron microscope equipped with a backscatter electron detector (BSED) and energy dispersive X-ray spectroscopy (EDS) detector, as well as the Tescan FIB FERA-3 Model GMH Scanning Electron Microscope that was used for Xe beam etching.

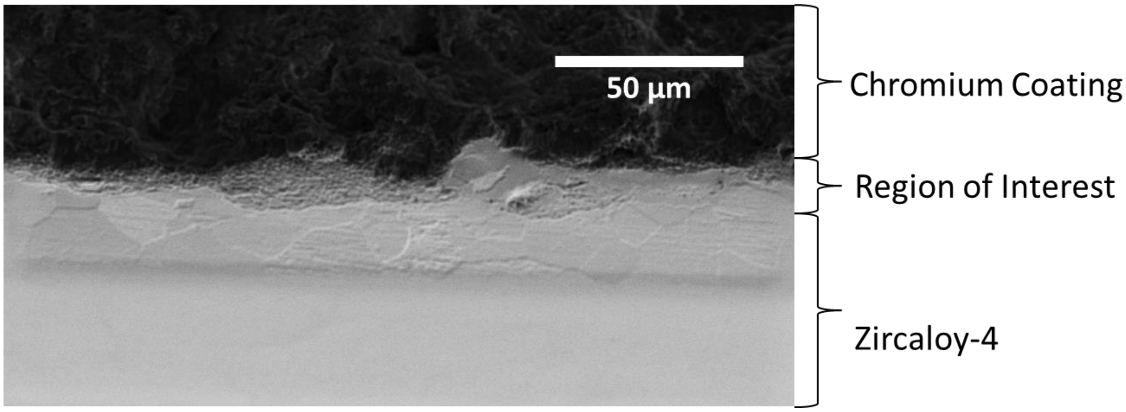

Figure 39. Cr diffusion zone following 0.04 um solution polishing and localized 100 nm Xe beam etching.

The FERA-3 was also equipped with an EBSD detector and was used to map grain boundary orientations at the coating-cladding interface region to help provide uniform mechanical testing results.

Micropillar fabrication was performed with a Tescan FIB LYRA-3 Model GMH Scanning Electron Microscope with a Ga focused ion beam. These pillars were not fabricated with the ion lathe approach [25] taken in Section 2 Subsection 2.3, as the intention for these micropillars was to create short, tapered pillars with a lower aspect

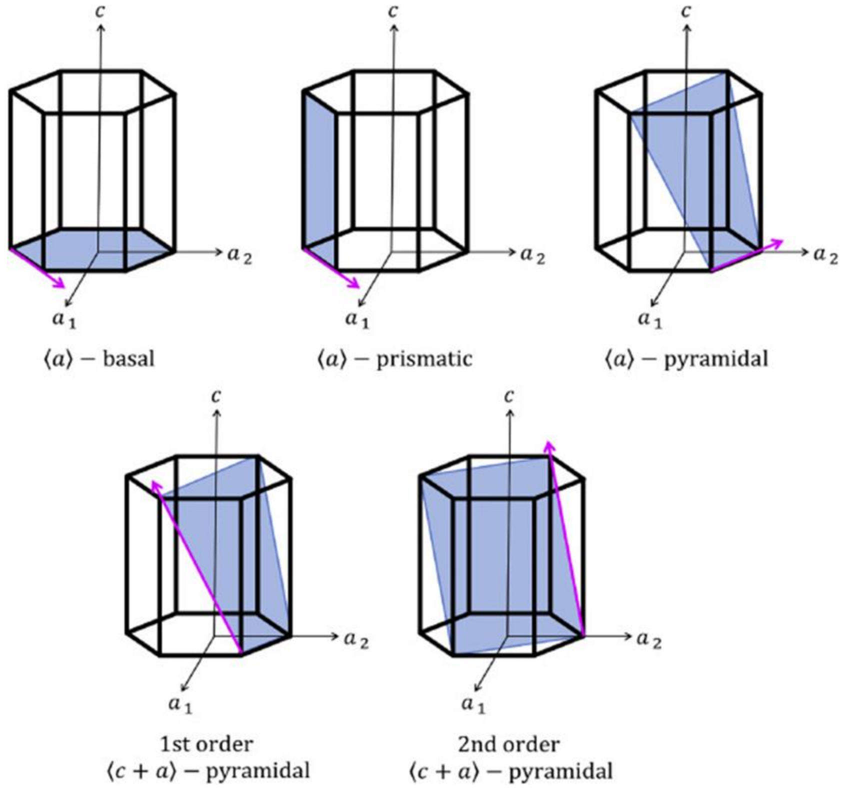

Figure 40. Slip planes of the HCP structure of Zircaloy-4. Reprinted under open access from [64] Copyright 2016 by Elsevier.

ratio in order to promote slip along the pyramidal planes of the HCP structure of Zircaloy-4, shown in Figure 40, following flat punch indentation on the (0001) basal plane. Final pillar dimensions were 2 µm tall, with a 2:1 aspect ratio (Figure 41). The final diameter of the pillars (1.0 µm) was selected as this was the maximum width of the Cr diffusion zone.

Micromechanical testing to study the mechanical properties of the intermetallic phases was performed using a Hysitron TI950 Triboindenter, equipped with a flat-punch probe for micropillar compression.

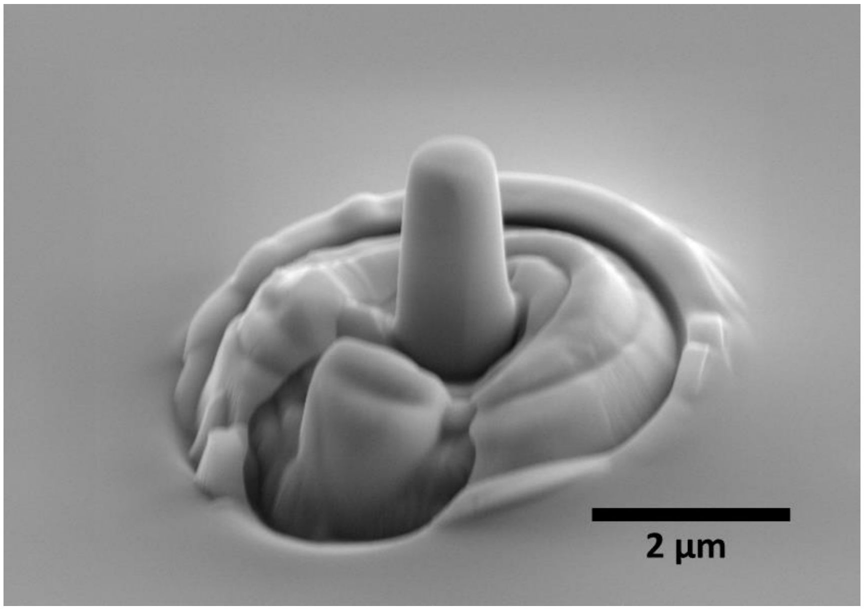

Figure 41. Micropillar fabricated in Zircaloy-4 bulk via FIB.

4.2 Premise and Challenges for Analysis

The initial goal for the analysis of the interface reactions of pure Cr-coated Zircaloy-4 was to follow a similar procedure to those outlined in Sections 2 and 3. However, it was quickly found that the diffusion of Cr into the Zircaloy-4 rapidly saturated at an average phase thickness of 1.1 μm. The SEM BSED images of Figure 42a and Figure 42b compare the interphase growth after three and six weeks. The interphase is visible as the intermediate shade of grey between the Cr (top) and Zircaloy-4 (bottom).

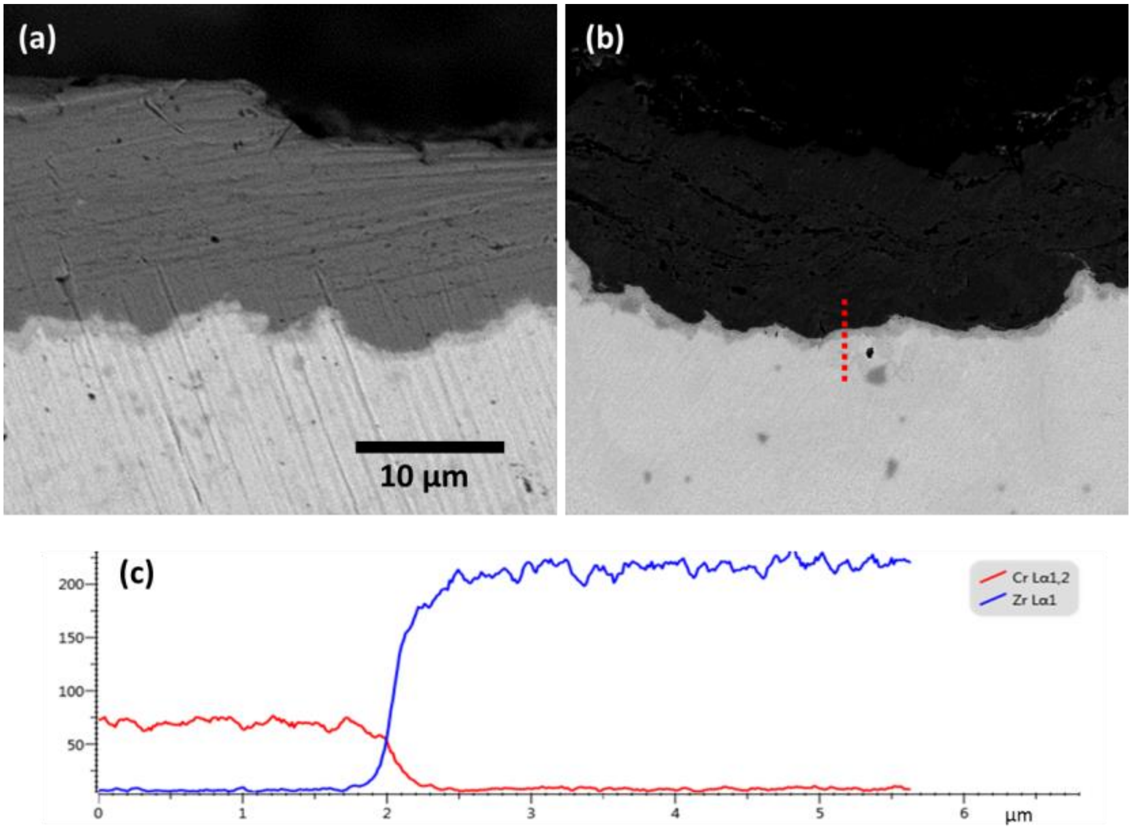

Figure 42. SEM BSED images of (a) pure Cr-coated Zircaloy-4 after three weeks of annealing at 998 K; (b) after six weeks of annealing at 998 K. (c) EDS line scan data at the dotted red line in (b).

This saturation makes the same diffusion kinetic analysis in Sections 2 and 3 impossible. Additionally, EDS line scans across this interface region (Figure 42c) revealed no discernable intermetallic growth. Instead, what was seen was a linear diffusion of Cr into Zr. The linear extent of the interdiffusion from Figure 42c matches the 1.1 µm phase thickness evaluated from measuring the phase width in Figure 42b.

Figure 43 shows an SEM secondary electron (SE) image of the interface zone. Note that SE images of this region do not visually show the diffusion zone as effectively as BSED images. Dotted lines were added to the image to better show the approximate

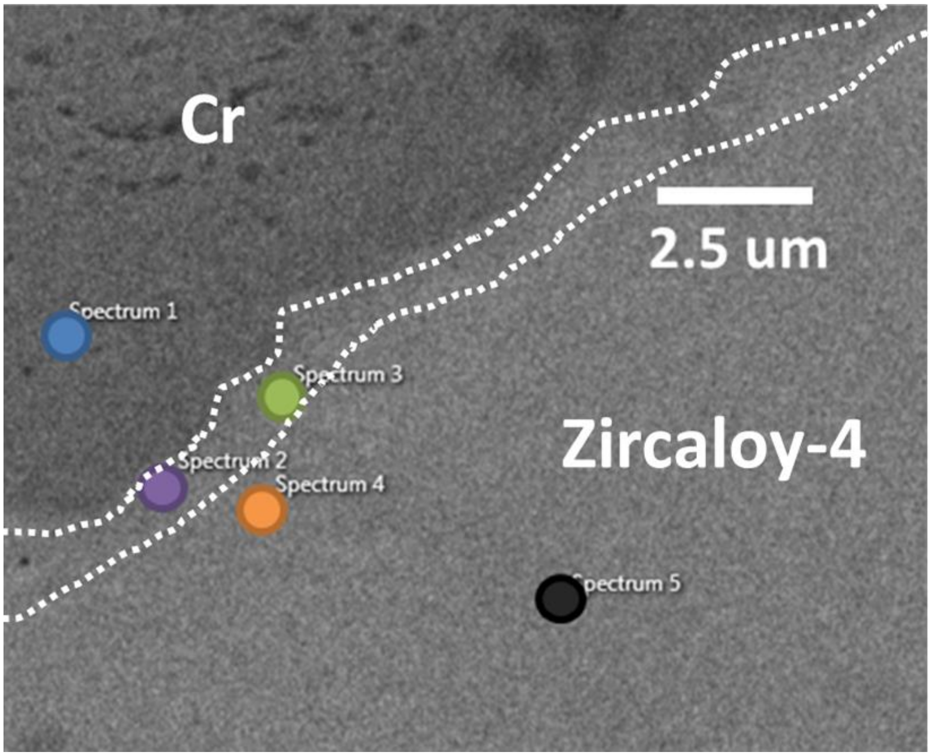

Figure 43. SEM SE image of the Cr-Zircaloy-4 interface region. Colored dots correspond to EDS point scans across the system. Dotted white lines indicate the approximate extent of Cr diffusion zone.

width of the diffuse region The colored dots in the figure correspond to EDS point scans of the interface zone. The data for these scans is presented in Table 4.

Table 4. EDS Point Scans across the interface zone in Figure 43.

Point	**Blue**	**Purple**	**Green**	**Orange**	**Black**
Cr at %	100.0	13.9	8.3	1.6	1.6
Zr at %	0%	86.1	91.7	98.4	2.9

The data in Table 4 confirm the finding from the EDS line scan in Figure 42c that there is no single Zr_xCr_y phase that has formed between the Cr and Zircaloy-4, even after six weeks at 998 K. However, the phase diagram in Figure 37 [63] predicts the existence of a $ZrCr_2$ eutectic phase. It is noted that this phase could exist in the annealed samples, but given the linear diffusion of Cr into Zircaloy-4 over 1.1 µm, would put this $ZrCr_2$ too small for the resolution of both SEM-EDS and STEM-EDS to be effective at positive identification, and well below the average size of grains noted in the diffuse zone (~10-20 µm).

Numerous problems were quickly found for mechanical properties testing. The Cr-diffuse region was extremely thin at only 1.1 µm thick on average, making precise results with conventional nanoindentation impossible. FIB is precise enough to fabricate 1.0 µm in diameter micropillars in this diffuse zone, therefore micropillar compression was attempted to test the mechanical properties of the diffusion zone versus the bulk

Zircaloy-4. The load at which pillars fractured was to be compared between pillars fabricated in the Cr-diffuse region and the Zircaloy-4 bulk, both before and after ion irradiation. Initially, test micropillars made in the Zircaloy-4 bulk presented significantly different results upon compression. Three pillars were tested, with the first fracturing at 1800 µN of indenter load, the second not fracturing even past 10,000 µN of load, and the final fracturing after 4100 µN of load. This large discrepancy was attributed to the pillars being made on grain boundaries or on grains of different orientation relative to the indenter. Therefore, for uniformity of test conditions, micropillars had to be made on single grains of similar grain orientation with respect to the indentation direction. EBSD was necessary to identify such grains.

The initially-used polishing technique of using 0.25 µm diamond solution was found to be insufficient for EBSD. This polish quality is shown in Figure 38, and was too rough to identify Kikuchi lines with the EBSD detector. A supplemental polishing step using 0.04 µm diamond solution was added, but any grains in the Zircaloy-4 or the diffuse region exposed by polishing were immediately obscured by passive oxide layer formation, preventing EBSD mapping. A FIB Xe beam was used for etching to remove the oxide layer, with the end result being a sample surface smooth enough for successful EBSD mapping. Figure 39 shows the Cr-diffuse region following these polishing steps, and Figure 44 shows the resulting EBSD grain mapping. However, the ultra-fine precision required of the final polishing step resulted in a lack of reproducibility for the desired quality, as even minor imperfections of the polishing pad carrying the solution could render the surface unusable during polishing.

To add an additional consideration, the desired surface finish can only survive two or three Xe etching attempts to remove the oxidation layer and expose grains for EBSD. Once a Xe-etched sample is removed from vacuum, ZrO_2 develops in the etched region, removing Zr atoms from the surface grains of the Cr-diffuse Zircaloy-4 and degrading surface finish. Over enough vacuum and etching cycles, the polished surface quality of the Zircaloy-4 is destroyed, and repolishing is required. Crucially, this means that any ion-irradiated samples have a limited number of EBSD mapping attempts, as the irradiated near-surface region is entirely removed if the surface finish is destroyed and the sample needs to be repolished.

While it is possible to select any grain orientation for pillar fabrication and attempt compression tests (with the exception of indenting directly on a prismatic plane, as this results in several slips or fractures as the pillar compresses vertically in steps,

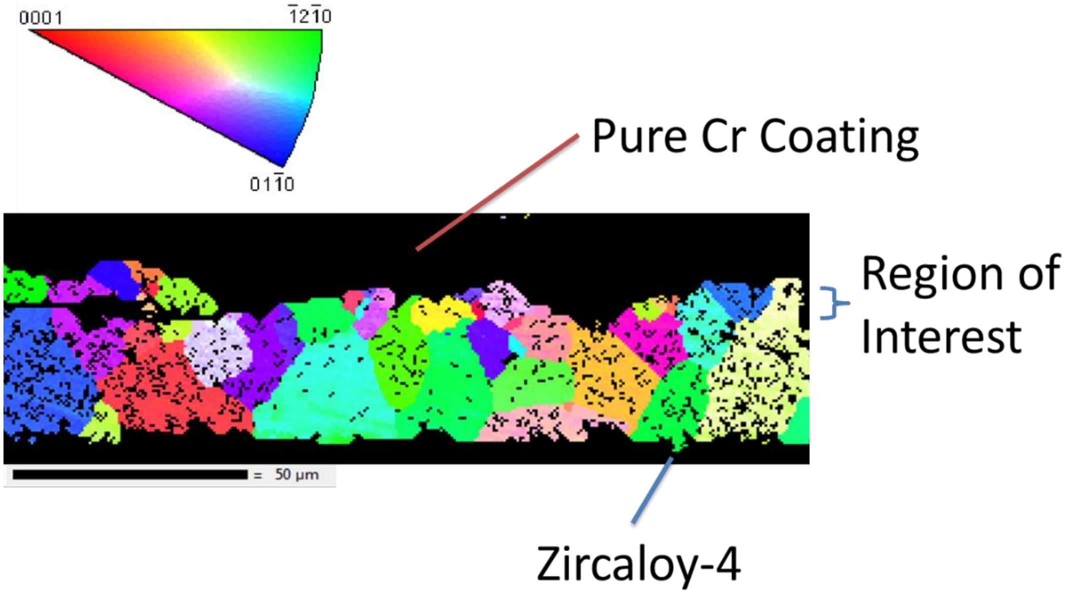

Figure 44. EBSD grain orientation map of the Cr-diffuse region.

compared to a single distinct fracture), it was immediately evident that the total number of pillars fabricated in this instance were not high enough to create good statistical results. In order for a grain to be suitable for pillar fabrication, the grain must be within that 1.1 µm diffusion range, be of the desired orientation, and be sufficiently large enough for positive visual identification under SEM (identifying a suitable grain in EBSD is not helpful if the grain is too small to be seen or is visually indistinguishable from grains surrounding it). These limiting criteria make suitable grains for fabricating micropillars exceedingly rare. Therefore, inducing pyramidal slips on fabricated micropillars was the desired approach. A single crystal lattice slip provides good uniformity in fracture load, as this type of slip results in no structural deformation of the pillar before fracture. By eliminating structural deformation before fracture, the impact of pillar buckling and random defects already present in the lattice are largely negated, eliminating sources of random error, resulting in fewer tests necessary for desirable final statistics.

As mentioned in Section 4, Subsection 4.1, grains with the basal (0001) plane oriented vertically with respect to the indenter were selected, as the slip systems for load applied to the basal plane are pyramidal [64]. Successful EBSD mappings like the one shown in Figure 44 were used to identify grains with the (0001) plane oriented upwards, towards the indenter. Figure 45a shows a micropillar fabricated in the bulk Zircaloy-4 on a grain with this orientation, and Figure 45b shows this pillar following compression. In the case of the grains in Figure 44, only a single (0001) grain was large enough for positive identification and pillar fabrication, but it was not close enough to the diffuse region.

Perhaps most crucial of all is the consideration that the Cr-diffuse region is not a single phase of uniform Cr concentration. For example, a pillar created 100 nm from the Cr coating interface would be expected to comprise of approximately 89 at% Cr and 11 at% Zr, whereas a pillar created 500 nm from the Cr interface would be approximately 45 at% Cr and 55 at% Zr. Given the already limiting rarity of suitable grains for pillar fabrication, realistically no consideration could afford to be given to maintaining uniform distance from the Cr coating interface.

To summarize the challenges in assessing mechanical properties of the Cr-diffuse region: conventional nanoindentation is impossible due to the 1.1 μm thickness of this region, micropillar compression is only viable on grains within this narrow region that are the correct size and orientation, micropillar fabrication is only possible after an extensive polishing procedure with poor reproducibility, and there is no single intermetallic phase present in this diffuse region that provides any uniformity in testing results.

When looking at the Cr-Zircaloy-4 interface zone as a whole, however, it is evident that the impact of this relatively mild intermetallic diffusion is bound to be more limited than the impact created by the more complex intermetallic interactions at the FeCrAl-Zircaloy-4 and TiAlC-Zircaloy-4 interface zones. In fact the Cr interdiffusion is more likely to reinforce the coating's adhesion to Zircaloy-4. Ultimately, more research into the potential impact this Cr-diffuse zone has on the coating-cladding interface is needed.

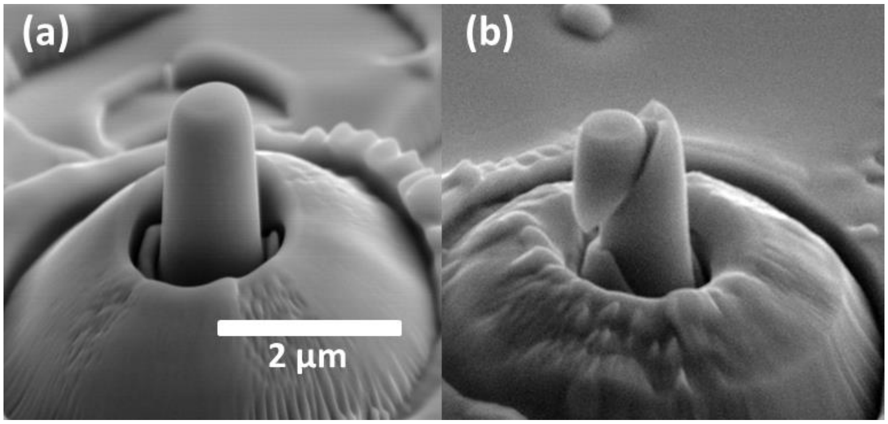

Figure 45. (a) Micropillar fabricated in a bulk Zircaloy-4 grain with the (0001) plane oriented towards the indenter. (b) This pillar following compression.

5. CONCLUSIONS

The conclusions drawn from this research indicates clearly that independent study of Zircaloy-4 and prospective coatings is not entirely sufficient for predicting the practical implications of the long-term use of coated fuel cladding. This study concluded that when coupled in high-temperature environments, intermetallic materials formed between the coatings and substrate, and these intermetallics possessed differing material properties and irradiation response to the coating and cladding. A cold-spray coating technique developed by the University of Madison-Wisconsin [7] was used to coat the Zircaloy-4 with $Fe_{70}Cr_{20}Al_{10}$, Ti_2AlC, and pure Cr. The coated Zircaloy-4 was annealed in high vacuum to promote metallic interdiffusion between the coating and the Zircaloy-4.

In the case of the FeCrAl-coated Zircaloy-4, following three weeks of vacuum annealing at 998 K, SEM characterization revealed the formation of the intermetallics $(Fe,Cr)_2Zr$/ Fe_2Zr and Zr_3Fe. The intermetallic compound widths were measured and the activation energies for the mixed Fe_2Zr intermetallic and the Zr_3Fe intermetallic were calculated to be 65 kJ/mol and 58 kJ/mol, respectively [21]. The adhesion strength of the cold-spray technique was tested by cantilever bending of cantilevers fabricated at the coating-cladding interface. The test showed adhesion strength of the cold-spray process exceeded the mechanical strength of the FeCrAl coating. This was concluded after the coating mechanically failed before the interface separated. Nanoindentation testing showed that two intermetallics were significantly higher than either the substrate or the coating. Micropillars in each of the intermetallics were fabricated and compression tests were performed. Zircaloy-4 exhibited ductile deformation behavior as expected, but the two intermetallics and the FeCrAl coating both showed brittle failure. FeCrAl was expected to show ductile failure, however it is speculated that defects introduced from the cold-spray process transitioned the coating from a ductile to brittle failure mode [21]. Additionally, the cold-spray process created porosity in the FeCrAl coating (also observed in TiAlC). These are indications that refinement to the cold-spray process are necessary.

The $(Fe,Cr)_2Zr$/ Fe_2Zr phase was found to contain ZrC and FeCrAl impurities, appearing as small grains. The source of the ZrC is attributed to SiC polishing during surface preparation for cold-spraying. After irradiation with 3.5 MeV Zr^{2+} ions to 50, 100, and 150 peak dpa, no void swelling was observed in all intermetallics, the coating, and substrate. ZrC showed good radiation tolerance and, despite ceramics being generally vulnerable to irradiation-induced amorphization, did not amorphize. However, the intermetallic $(Fe,Cr)_2Zr$ became completely amorphized after ion irradiation, likely due to its high glass formation capability [21]. This phase change presents a significant risk of delamination over the lifetime of the fuel rod, and this suggests that further evaluation on the impact of $(Fe,Cr)_2Zr$ formation on overall coating-cladding structural integrity is needed.

In the case of the TiAlC-coated samples, annealing at 923 K for 314 hours resulted in the intermetallics Zr_3Al, ZrAl, and $ZrAl_2$ to form between the coating and substrate. Additionally, $(Fe,Cr)_2Zr$ was found to precipitate in the intermetallic Zr_3Al. $ZrAl_2$ and Zr_3Al were observable after 168 hours of annealing at 923 K, followed ZrAl at 314 hours. The phase widths were measured via SEM-BSED imaging, and the activation energy of the diffusing aluminum was calculated to be 202 kJ/mol [46].

After ion irradiation via 3.5 MeV Zr^{2+} ions to 100 peak dpa, the hardness of the TiAlC coating, Zr_3Al, and Zircaloy-4 were noted to increase, while the ZrAl and $ZrAl_2$ region retained the same hardness. All three intermetallics showed partial amorphization following the ion irradiations, and the $(Fe,Cr)_2Zr$ precipitates in Zr_3Al fully amorphized. The hardness increase is attributed to the increase of dislocation density in the coating, substrate, and Zr_3Al, while the lack of hardness change in the ZrAl and $ZrAl_2$ region indicates that the amorphous phase of these materials are similar in hardness to their nanocrystalline phases.

These results suggest that for TiAlC coated Zircaloy-4, the intermetallic phases that form will undergo structural and phase changes over the duration of their usable lifetimes. This suggests a need for further systematic studies in order to better understand the impact of irradiation on the structural stability of TiAlC-coated Zircaloy-4 in reactor environments.

Lastly, in the case of the pure Cr-coated samples, after annealing at 998 K for 504 hours, Cr diffused linearly into Zircaloy-4 over a region 1.1 µm thick on average. Notably, after a further 504 hours of annealing, this 1.1 µm thick region did not appear to grow, implying that Cr diffusion into Zircaloy-4 saturated after three weeks. As a result, any diffusion kinetic analysis would not provide substantive results. Additionally, despite predictions from the Cr-Zr phase diagram [63], no discernable Zr_xCr_y intermetallic formed at the interface after 1008 hours of annealing at 998 K.

The thin width of this 1.1 µm Cr-diffuse region made conventional micromechanical testing either impossible or provide poor reproducibility. Nanoindentation cannot be performed accurately on a region that small, but micropillar fabrication and compression testing were possible. Preliminary micropillar compression testing indicated that the load at which fracture of the pillars occurred can fluctuate extensively for pillars made at random locations. As a result, EBSD was utilized to identify individual grains and grain orientations, with the intent being that selecting a specific grain orientation on which to fabricate pillars would provide uniformity in the results. However, if the Cr-diffuse region was to be investigated, pillars needed to have been made on exceedingly rare grains within the diffuse region, limiting the number of compression tests possible, rendering results from such testing far too statistically inaccurate to be viable. Ultimately, the apparent absence of any observable intermetallic coupled with the thin width of the Cr-diffuse region implies that there are no significant structural or mechanical property changes expected at the interface of the Cr-Zircaloy-4 system, especially when compared to the particularly complex intermetallic phase formations in the FeCrAl and TiAlC-coated samples.

REFERENCES

[1] Live Broadcast from Fukushima Central Television, Fukushima, Japan, Broadcast on March 11, 2011.

[2] P. Sofronis and H. Birnbaum, "Mechanics of the hydrogen-dislocation-impurity interactions—I. Increasing shear modulus," *J. Mech. Phys. Solids* , vol. 43, pp. 49-90, 1995.

[3] C. D. Beachem, "A new model for hydrogen-assisted cracking (hydrogen “embrittlement”)," *Metall. and Mater. Trans. B,* vol. 3, no. 2, pp. 441-455, 1972.

[4] T. R. Allen, R. J. M. Konings and A. T. Motta, "Corrosion of Zirconium Alloys," *Comprehensive Nuclear Materials,* vol. 5, pp. 49-68, 2012.

[5] K. G. Field, S. A. Briggs, P. D. Edmondson, J. C. Haley, R. H. Howard, X. Hu, K. C. Littrell, C. M. Parish and Y. Yamamoto, "Database on Performance of Neutron Irradiated FeCrAl Alloys," Oak Ridge National Laboratory, 2016.

[6] B. Diaz, L. Olson, C. Verst, R. Sindelar, E. Hoffman, B. Hauch, B. Maier and K. Sridharan, "MAX Phase Coatings for Accident Tolerant Nuclear Fuel," *Trans. of the Amer. Nucl. Soc.,* vol. 110, pp. 994-996, 2014.

[7] B. Maier, B. Garcia-Diaz, B. Haunch, L. C. Olson, R. L. Sindelar and K. Sridharan, "Cold Spray Deposition of Ti2AlC coatings for improved nuclear fuel cladding," *J. Nucl. Mater.* , vol. 466, pp. 712-717, 2015.

[8] G. S. Was, Fundamentals of Radiation Materials Science: Metals and Alloys, New

York: Springer, 2007.

[9] L. R. Greenwood, "Neutron interactions and atomic recoil spectra," *J. Nucl. Mater.,* vol. 216, p. 29, 1994.

[10] F. A. Garner, "Impact of the injected interstitial on the correlation of charged particle and neutron-induced radiation damage," *J. Nucl. Mater.,* vol. 117, pp. 177-197, 1983.

[11] J. G. Gigax, H. Kim, E. Aydogan, F. A. Garner, S. Maloy and L. Shao, "Beam-contamination-induced compositional alteration and its neutron-atypical consequences in ion simulation of neutron-induced void swelling," *Mater. Res. Let.,* vol. 5, no. 7, pp. 478-485, 2017 .

[12] K. A. Terrani, J. J. Powers and N. M. George, "Neutronic analysis of candidate accident-tolerant iron alloy cladding concepts," *Trans. of the Amer. Nucl. Soc.,* vol. 109, pp. 1508-1508, 2013.

[13] S. Chen and C. Yuan, "Neutronic Analysis on Potential Accident Tolerant Fuel-Cladding Combination U3Si2-FeCrAl," *Science and Tech. of Nucl. Install.,* vol. 2017, p. 3146985, 2017.

[14] A. J. Rothman, "Potential Corrosion and Degradation Mechanisms of Zircaloy Cladding on Spent Nuclear Fuel in a Tuff Repository," Lawrence Livermore National Laboratory, Livermore, 1984.

[15] "University of Wisconsin Cold Spray Program," University of Wisconsin-Madison, 2011. [Online]. Available: http://coldspray.ep.wisc.edu/program.html.

[16] C. Servant, C. Gueneau and I. Ansara, "Experimental and Thermodynamic Assessment of the Fe-Zr System," *J. Alloys & Compds.*, vol. 220, p. 19, 1995.

[17] J. Ziegler, M. Ziegler and J. Biersack, "SRIM- The Stopping Range of Ions in Matter," *Nucl. Instr. Meth. Phys. Res. B*, vol. 268, 2010.

[18] L. Shao, J. Gigax, D. Chen, H. Kim, F. Garner, J. Wang and M. Toloczko, "Standardization of Accelerator Irradiation Procedures for Simulation of Neutron Induced Damage in Reactor Structural Materials," *Nucl. Instr. Meth. Phys. Res. B,* vol. 254, pp. 251-254, 2017.

[19] K. G. Field, M. A. Snead, Y. Yamamoto and K. A. Terrani, "Handbook on the Material Properties of FeCrAl Alloys for Nuclear Power Production Applications," Oak Ridge National Laboratory, 2017.

[20] F. Stein, G. Sauthoff and M. Palm, "Experimental Determination of Intermetallic Phases, Phase Equilibria, and Invariant Reaction Temperatures in the Fe-Zr System," *J. Phase Equilib.*, vol. 23, p. 480, 2002.

[21] J. G. Gigax, M. Kennas, H. Kim, B. R. Maier, H. Yeom, G. O. Johnson, K. Sridharan and L. Shao, "Interface Reactions and Mechanical Properties of FeCrAl-Coated Zircaloy-4," *J. Nucl. Mat.*, vol. 519, pp. 57-63, 2019.

[22] C. Matano, "On the Relation Between Diffusion-Coefficients and Concentrations of Solid Metals (The Nickel-Copper System)," *Japanese J. of Phys.* , vol. 8, 1933.

[23] C. Wagner, "The Evaluation of Data Obtained with Diffusion Couples of Binary Single-Phase and Multiphase Systems," *Acta Metall.,* vol. 17, p. 99, 1969.

[24] K. Bhanumurthy, G. B. Kale and S. K. Kera, "Reaction Diffusion in the Zirconium-Iron System," *J. Nucl. Mater.,* vol. 185, pp. 208-213, 1991.

[25] D. D. Maio and S. G. Roberts, "Measuring Fracture Toughness of Coatings Using Focused-Ion-Beam-Machined Microbeams," *J. Mater. Res.,* vol. 20, pp. 299-302, 2005.

[26] W. Oliver and G. M. Pharr, "An Improved Technique for Determining Hardness and Elastic Modulus Using Load and Displacement Sensing Indentation Experiments," *J. Mater. Res.,* vol. 7, pp. 1564-1583, 1992.

[27] A. Garde, H. M. Chung and T. F. Kassner, "Uniaxial Tensile Properties of Zircaloy Containing Oxygen," Argone National Lab, 1977.

[28] J. B. Bai, C. Prioul and D. Francois, "Hydride Embrittlement in Zircaloy-4 Plate: Part I. Influence of Microstructure on the Hydride Embrittlement in Zircaloy4 at 20 C and 350 C," *Metall. Mater. Trans.,* vol. 25, pp. 1185-1197, 1994.

[29] C. A. Volkert and E. Lilleodden, "Size Effects in the Deformation of Sub-Micron Au Columns," *Phil. Mag.,* vol. 86, pp. 5567-5579, 2006.

[30] M. D. Uchic, D. M. Dimiduk, J. N. Florando and W. D. Nix, "Sample Dimensions Influence Strength and Crystal Plasticity," *Science,* vol. 305, pp. 986-989, 2004.

[31] Y. Yamamoto, B. A. Pint, K. A. Terrani, K. G. Field, Y. Yang and L. L. Snead, "Development and Property Evaluation of Nuclear Grade Wrought FeCrAl Fuel Cladding for Light Water Reactors," *J. Nucl. Mater.,* vol. 467, pp. 703-716, 2015.

[32] R. W. Gilbert, M. Griffiths and G. J. C. Carpenter, "Amorphous intermetallics in

neutron irradiated zircaloys after high fluences," *J. Nucl. Mater.*, vol. 135, pp. 265-268, 1985.

[33] M. Griffiths, R. W. Gilbert and G. J. C. Carpenter, "Phase instability, decomposition and redistribution of intermetallic precipitates in Zircaloy-2 and -4 during neutron irradiation," *J. Nucl. Mater.*, vol. 150, pp. 53-66, 1987.

[34] A. T. Motta and D. R. Olander, "Theory of electron-irradiation-induced amorphization," *Acta. Metall. Mater.*, vol. 38, pp. 2175-2185, 1990.

[35] L. M. Howe, D. Phillips, A. T. Motta and P. R. Okamoto, "Irradiation-induced phase transformations in zirconium alloys," *Sur. and Coatings Tech.*, vol. 66, pp. 411-418, 1994.

[36] A. Aitkaliyeva, L. Shao, L. Price, J. Gigax, H. Kim, D. A. Lucca, A. Zare, E. G. Fu and G. Xie, "Ordered nanocrystal formation in Cu50Zr45Ti5 metallic glass," *Beam Inter. with Mater. and Atoms*, vol. 448, pp. 57-60, 2019.

[37] M. Myers, E. Fu, H. Wang, G. Xie, X. Wang, W. Chu and L. Shao, "An experimental and modeling study on the role of damage cascade formation in nanocrystallization of ion-irradiated Ni52.5 Nb10 Zr15 Ti15 Pt7.5 metallic glass," *Scripta Metarialia*, vol. 63, pp. 1045-1048, 2010.

[38] L. Shao, D. Chen, M. Myers, J. Wang, B. Tilakaratne, D. Wijesundera, W.-K. Chu, G. Xie, A. Zare and D. A. Lucca, "Smoothing metallic glasses without introducing crystallization by glass cluster ion beam," *Appl. Phys. Lett.*, vol. 102, p. 101604, 2013.

[39] H. Ihara, M. Hirabayashi and H. Nakagawa, "Electronic band structures and x-ray photoelectron spectra of ZrC, HfC, and TaC," *Phys. Rev. B,* vol. 14, no. 4, p. 1707, 1976.

[40] R. Andrievskii, V. Savin, V. Y. Markin, V.T.Spravtsev and A. Shevshenko, *Inorg. Mater.,* vol. 14, no. 4, p. 526, 1978.

[41] D. Gosset, M. Dollé, D. Simeone, G. Baldinozzi and L. Thomé, "Structural evolution of zirconium carbide under ion irradiation," *J. Nucl. Mater.,* vol. 373, pp. 123-129, 2008.

[42] J. C. Haley, S. A. Briggs, P. D. Edmondson, K. Sridharan, S. G. Roberts, S. Lozano-Perez and K. G. Field, "Dislocation loop evolution during in-situ ion irradiation of model FeCrAl alloys," *Acta Mater.,* vol. 136, pp. 390-401, 2017.

[43] K. Lambrinou, T. Lapauw, B. Tunca and J. Vleugels, "MAX Phase Materials for Nuclear Applications," *Ceramic Engineering and Science Proceedings,* vol. 37, pp. 223-233, 2017.

[44] M. W. Barsoum and M. Radovic, "Elastic and Mechanical Properties of the MAX Phases," *Annual Review of Materials Research,* vol. 41, pp. 195-227, 2011.

[45] K. H. Beckurts and K. Wirtz, Neutron Physics, Berlin: Springer-Verlag Berlin - Gottingen - Heidelberg , 1958.

[46] J. G. Gigax, M. D. Kennas, H. Kim, T. Wang, Maier, B. R., H. Yeom, G. O. Johnson, K. Sridharan and L. Shao, "Radiation Response of Ti2AlC MAX phase coated Zircaloy-4 for accident tolerant fuel cladding," *Journal of Nuclear Materials,*

vol. 523, pp. 26-32, 2019.

[47] C. Li, J. She, M. Pang and W. Yang, "Phase Equilibria in the Al-Zr-Nd System at 773 K," *Journal of Phase Equilibria and Diffusion,* vol. 32, pp. 24-29, 2011.

[48] J. C. Rao, Y. T. Pei, H. J. Yang, G. M. Song, S. B. Li and J. T. M. D. Hosson, "TEM study of the initial oxide scales of Ti2AlC," *Acta Mater.,* vol. 59, pp. 5216-5223, 2011.

[49] G. V. Kidson and G. D. Miller, "A study of the Interdiffusion of Aluminum and Zirconium," *J. Nucl. Mater.,* vol. 12, pp. 61-69, 1964.

[50] A. Laik, K. Bhanumurthy and G. B. Kale, "Intermetallics in the Zr-Al Diffusion Zone," *Intermetallics,* vol. 36, pp. 175-178, 1985.

[51] J. Carr, G. Vasudevamurthy, L. Snead, B. Hinderliter and C. Massey, "Investigations of Aluminum-Doped Self-Healing Zircaloy Surfaces in Context of Accident Tolerant Fuel Cladding Research," *J. Mater. Engineer. and Perf.,* vol. 25, pp. 2347-2355, 2016.

[52] Z. J. Lin, M. J. Zhuo, Y. C. Zhou, M. S. Li and J. Y. Wang, "Microstructural Characterization of Layered Ternary Ti2AlC," *Acta Mater.,* vol. 54, pp. 1009-1015, 2006.

[53] F. Hofmann, R. J. Harder, W. Liu, Y. Liu, I. K. Robinson and Y. Zayachuk, "Glancing-incidence focussed ion beam milling: a coherent X-ray diffraction study of 3D nano-scale lattice strains and crystal defects," *Acta Mater.,* vol. 154, pp. 113-123, 2018.

[54] C. G. Wilson, "The Crystal Structure of ZrAl2," *Acta Cryst.*, vol. 12, p. 660, 1959.

[55] F. J. Spooner and C. G. Wilson, "The Crystal Structure of ZrAl," *Acta Cryst.*, vol. 15, p. 621, 1962.

[56] L. M. Howe and M. H. Rainville, "A study of the irradiation behavior of Zr3Al," *J. Nucl. Mater.*, vol. 68, pp. 215-234, 1977.

[57] J. Koike, P. R. Okamoto, L. E. Rehn and M. Meshii, "Amorphization in Zr3Al irradiated with 1 MeV e- and Kr+," *Metall. Trans. A.*, vol. 21, pp. 1799-1808, 1990.

[58] E. M. Schulson, "The strengthening of ordered Zr3Al by fast neutron irradiation," *Acta Metall.*, vol. 26, p. 1189, 1978.

[59] H. E. Rosinger, "Effect of fast neutron irradiation on the properties of Zr3Al-based alloys," *J. Nucl. Mater.*, vol. 95, p. 171, 1980.

[60] A. J. Ardell, "Ion-irradiated intermetallic compounds," *Mater. Sci. and Eng.*, vol. 152, pp. 212-226, 1992.

[61] M. Ševeček, A. Gurgen, A. Seshadri, Y. Che, M. Wagih, B. Phillips, V. Champagne and K. Shirvan, "Development of Cr cold spray–coated fuel cladding with enhanced accident tolerance," *Nucl. Eng. and Tech.*, vol. 50, no. 2, pp. 229-236, 2018.

[62] R. Wadsack, R. Pippan and B. Schedler, "Structural refinement of chromium by severe plastic deformation," *Fusion Engineering and Design*, vol. 66, pp. 265-269, 2003.

[63] H. J. Lu, W. B. Wang, N. Zou, J. Y. Shen, X. G. Lu and Y. L. He, "Thermodynamic Modeling of Cr-Nb and Zr-Cr with Extension to the Ternary Zr-Nb-Cr System,"

CALPHAD, vol. 50, pp. 134-143, 2015.

[64] Z. Zhang, D. Balint and F. Dunne, "Rate sensitivity in discrete dislocation plasticity in hexagonal close-packed crystals," *Acta Mater.*, vol. 107, pp. 17-26, 2016.